

Karady, George G. "Transmission System"  
*The Electric Power Engineering Handbook*  
Ed. L.L. Grigsby  
Boca Raton: CRC Press LLC, 2001

[www.ControlMakers.ir](http://www.ControlMakers.ir)

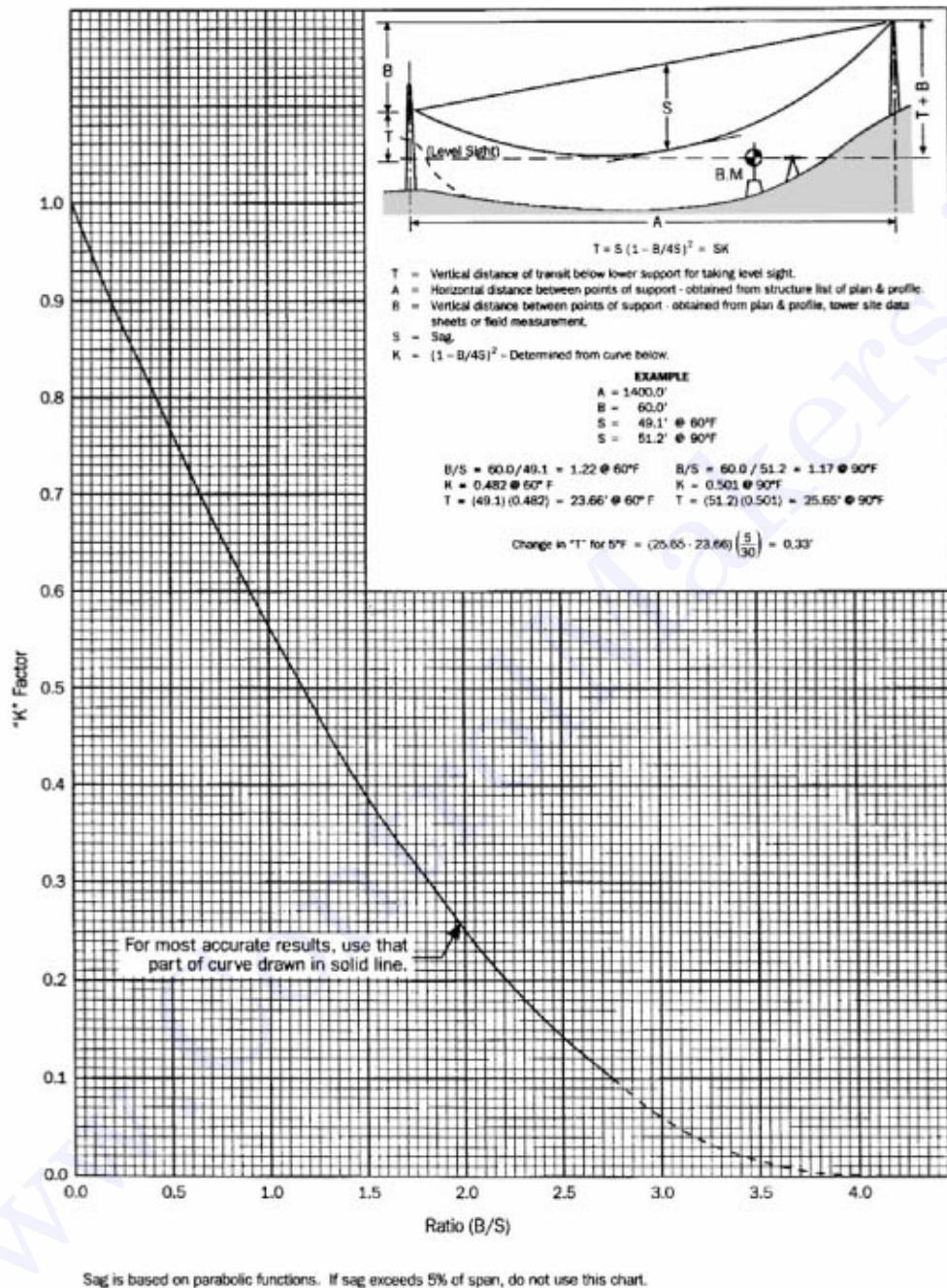
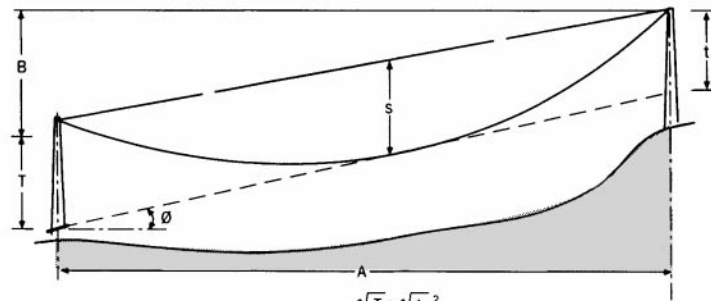


FIGURE 4.80 Conductor sagging by horizontal line of sight.

**Running board:** A pulling device designed to permit stringing more than one conductor simultaneously with a single pulling line. For distribution stringing, it is usually made of lightweight tubing with the forward end curved gently upward to provide smooth transition over pole cross-arm rollers. For transmission stringing, the device is either made of sections hinged transversely to the direction of pull or of a hard-nose rigid design, both having a flexible pendulum tail suspended from the



**METHOD 1:**  $S = \left( \frac{\sqrt{T} + \sqrt{t}}{2} \right)^2$

**METHOD 2:**  $S = \frac{B}{2} + \frac{t}{2} - \frac{tM}{8}$

- S = Sag
- t = Vertical distance below support to line of sight.
- =  $T \pm B - A \tan \phi$  when angle  $\phi$  is above horizontal.
- =  $T \pm B + A \tan \phi$  when angle  $\phi$  is below horizontal.
- T = Vertical distance below support for transit.
- B = Vertical distance between points of support - obtained from plan & profile, tower site data sheets or field measurement.
- + B when support ahead is higher.
- B when support ahead is lower.
- A = Horizontal distance between points of support - obtained from structure list or plan & profile
- $\phi$  = Angle of sight
- M = Determined from curve on Figure 2-17.

**EXAMPLES**

Given:

- A = 1400.0'
- B = 60.0'
- T = 40.0'
- $\phi = +1^\circ 40' 21'' @ 60^\circ F$   
(Field Measured)

**METHOD 1**

$$S = \left( \frac{\sqrt{T} + \sqrt{t}}{2} \right)^2$$

$$t = 40.0 + 60.0 - 1400.0 \tan 1^\circ 40' 21'' = 59.12'$$

$$\sqrt{t} = 7.689$$

$$\sqrt{T} = 6.325$$

$$S_{60^\circ F} = 49.1'$$

**METHOD 2**

Note: When using Method 2, value of "T" should lie between 3/4 "S" & 4/3 "S"

$$S = \frac{B}{2} + \frac{t}{2} - \frac{tM}{8}$$

$$t = 59.12'$$

$$t/2 = 29.56'$$

$$T/2 = 20.0''$$

$$M = 0.061$$

$$S_{60^\circ F} = 20.0 + 29.56 - \frac{(59.12)(0.061)}{8}$$

$$S_{60^\circ F} = 49.1'$$

Sag is based on parabolic functions. If sag exceeds 5% of span, do not use this chart.

FIGURE 4.81 Conductor sagging for checking sag S.

rear. This configuration stops the conductors from twisting together and permits smooth transition over the sheaves of bundle travelers.

*Synonyms:* alligator, bird, birdie, monkey tail, sled.

**Sag section:** The section of line between snub structures. More than one sag section may be required in order to properly sag the actual length of conductor which has been strung.

*Synonyms:* pull, setting, stringing section.

**Site, pull:** The location on the line where the puller, reel winder, and anchors (snubs) are located. This site may also serve as the pull or tension site for the next sag section.

*Synonyms:* reel setup, tugger setup.

**Site, tension:** The location on the line where the tensioner, reel stands and anchors (snubs) are located. This site may also serve as the pull or tension site for the next sag section.

*Synonyms:* conductor payout station, payout site, reel setup.

**Snub structure:** A structure located at one end of a sag section and considered as a *zero* point for sagging and clipping offset calculations. The section of line between two such structures is the sag section, but more than one sag section may be required in order to sag properly the actual length of conductor which has been strung.

*Synonyms:* 0 structure, zero structure.

**Tensioner, bullwheel:** A device designed to hold tension against a pulling line or conductor during the stringing phase. Normally, it consists of one or more pairs of urethane- or neoprene-lined, power braked, single- or multiple-groove bullwheels where each pair is arranged in tandem. Tension is accomplished by friction generated against the conductor which is reeved around the grooves of a pair of the bullwheels. Some tensioners are equipped with their own engines which retard the bullwheels mechanically, hydraulically, or through a combination of both. Some of these devices function as either a puller or tensioner. Other tensioners are only equipped with friction-type retardation.

*Synonyms:* retarder, tensioner.

**Tensioner, reel:** A device designed to generate tension against a pulling line or conductor during the stringing phase. Some are equipped with their own engines which retard the supporting shaft for the reel mechanically, hydraulically, or through a combination of both. The shaft, in turn, retards the reel. Some of these devices function as either a puller or tensioner. Other tensioners are only equipped with friction type retardation.

*Synonyms:* retarder, tensioner.

**Traveler:** A sheave complete with suspension arm or frame used separately or in groups and suspended from structures to permit the stringing of conductors. These devices are sometimes bundled with a center drum or sheave, and another traveler, and used to string more than one conductor simultaneously. For protection of conductors that should not be nicked or scratched, the sheaves are often lined with nonconductive or semiconductive neoprene or with nonconductive urethane. Any one of these materials acts as a padding or cushion for the conductor as it passes over the sheave. Traveler grounds must be used with lined travelers in order to establish an electrical ground.

*Synonyms:* block, dolly, sheave, stringing block, stringing sheave, stringing traveler.

**Winder reel:** A device designed to serve as a recovery unit for a pulling line. It is normally equipped with its own engine which drives a supporting shaft for a reel mechanically, hydraulically, or through a combination of both. The shaft, in turn, drives the reel. It is normally used to rewind a pulling line as it leaves the bullwheel puller during stringing operations. This unit is not intended to serve as a puller, but sometimes serves this function where only low tensions are involved.

*Synonyms:* take-up reel.

## References

Cahill, T., Development of Low-Creep ACSR Conductor, *Wire Journal*, July 1973.

Ehrenburg, D.O., Transmission Line Catenary Calculations, AIEE Paper, Committee on Power Transmission & Distribution, July 1935.

Fink, D.G. and Beaty, H.W., *Standard Handbook for Electrical Engineers*, 13th ed., McGraw-Hill.

*IEEE Guide to the Installation of Overhead Transmission Line Conductors*, IEEE Standard 524-1993, IEEE, New York, 1993.

*Graphic Method for Sag Tension Calculations for ACSR and Other Conductors*, Aluminum Company of America, 1961.

*Minimum Design Loads for Buildings and Other Structures*, American Society of Civil Engineers Standard, ASCE 7-88.

National Electrical Safety Code, 1993 edition.

Overend, P.R. and Smith, S., Impulse Time Method of Sag Measurement.

*Stress-Strain-Creep Curves for Aluminum Overhead Electrical Conductors*, Aluminum Association, 1974.

Winkelman, P.F., Sag-Tension Computations and Field Measurements of Bonneville Power Administration, AIEE Paper 59-900, June 1959.

## 4.8 Corona and Noise

*Giao N. Trinh*

Modern electric power systems are often characterized by generating stations located far away from the consumption centers, with long overhead transmission lines to transmit the energy from the generating sites to the load centers. From the few tens of kilovolts in the early years of the 20th century, the line voltage has reached the EHV levels of 800 kV AC (Lacroix and Charbonneau, 1968) and 500 kV DC (Bateman, 1969) in the 1970s, and touched the UHV levels of 1200 kV AC (Bortnik, 1988) and 600 kV DC (Krishnayya et al., 1988). Although overhead lines operating at high voltages are the most economical means of transmitting large amounts of energy over long distances, their exposure to atmospheric conditions constantly alters the surface conditions of the conductors and causes large variations in the corona activities on the line conductors.

Corona discharges follow an electron avalanche process whereby neutral molecules are ionized by electron impacts under the effect of the applied field (Raether, 1964). Since air is a particular mixture of nitrogen (79%), oxygen (20%), and various impurities, the discharge development is significantly conditioned by the electronegative nature of oxygen molecules, which can readily capture free electrons to form negative ions and thus hamper the electron avalanche process (Loeb, 1965). Several modes of corona discharge can be distinguished; and while all corona modes produce energy losses, the streamer discharges also generate electromagnetic interference, and audible noise in the immediate vicinity of HV lines (Trinh et al., 1968; Trinh, 1995). These parameters are currently used to evaluate the corona performance of conductor bundles and to predict the energy losses and environmental impact of HV lines prior to their installation.

Adequate control of line corona is obtained by controlling the surface gradient at the line conductors. The introduction of bundled conductors by Whitehead in 1910 has greatly influenced the development of HV lines to today's EHV voltages (Whitehead, 1910). In effect, HV lines as we know them today would not exist without the bundled conductors. This section reviews the physical processes leading to the development of corona discharges on the line conductors and presents the current practices in selecting the line conductors.

### Corona Modes (Trinh et al., 1968; Trinh, 1995)

In a nonuniform field gap in atmospheric air, corona discharges can develop over a whole range of voltages in a small region near the highly stressed electrode before the gap breaks down. Several criteria have been developed for the onset of corona discharge, the most familiar being the streamer criterion. They are all related to the development of an electron avalanche in the gas gap and can be expressed as

$$1 - \gamma \exp\left(\int \alpha' dx\right) = 0, \quad \text{with } \alpha' = (\alpha - \eta) \quad (4.133)$$

where  $\alpha'$  is the net coefficient of ionization by electron impact of the gas,  $\alpha$  and  $\eta$  are respectively the ionization and attachment coefficients in air, and  $\gamma$  is a coefficient representing the efficiency of secondary

processes in maintaining the ionization activities in the gap. The net coefficient of ionization varies with the distance  $x$  from the highly stressed electrode and the integral is evaluated for values of  $x$  where  $\alpha'$  is positive.

A physical meaning may be given to the above corona onset criteria. Rewriting the onset conditions as

$$\exp\left[\int(\alpha - \eta)dx\right] = \frac{1}{\gamma} \tag{4.134}$$

the left-hand side represents the avalanche development from a single electron and  $1/\gamma$ , the critical size of the avalanche to assure the stable development of the discharge.

The nonuniform field necessary for the development of corona discharges and the electronegative nature of air favor the formation of negative ions during the discharge development. Due to their relatively slow mobility, ions of both polarities from several consecutive electron avalanches accumulate in the low field region of the gap and form ion space charges. To properly interpret the development of corona discharges, account must be taken of the active role of these ion space charges, which continuously modify the local field intensity and, hence, the development of corona discharges according to their relative build-up and removal from the region around the highly stressed electrode.

### Negative Corona Modes

When the highly stressed electrode is at a negative potential, electron avalanches are initiated at the cathode and develop toward the anode in a continuously decreasing field. Referring to Fig. 4.82, the nonuniformity of the field distribution causes the electron avalanche to stop at the boundary surface  $S_0$  where the net ionization coefficient is zero, i.e.,  $\alpha = \eta$ . Since free electrons can move much faster than ions under the influence of the applied field, they concentrate at the avalanche head during its progression. A concentration of positive ions thus forms in the region of the gap between the cathode and the boundary surface, while free electrons continue to migrate across the gap. In air, free electrons rapidly attach themselves to oxygen molecules to form negative ions which, because of the slow drift velocity, start to

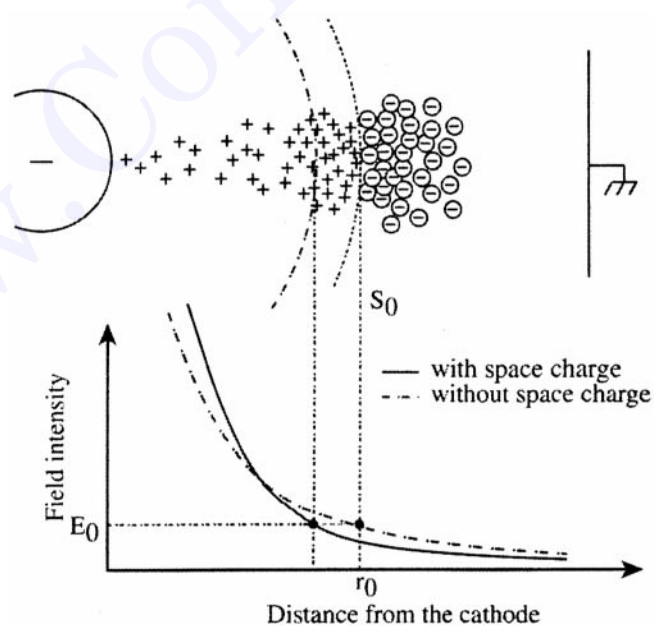
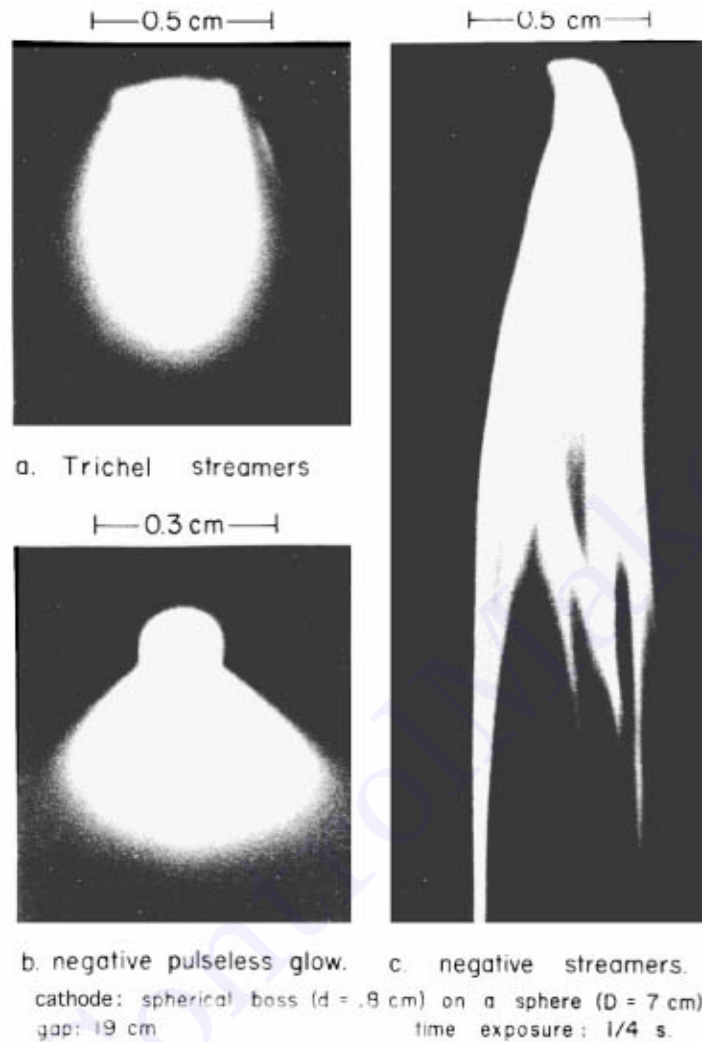


FIGURE 4.82 Development of an electron avalanche from the cathode. (Trinh, 1995.)



**FIGURE 4.83** Corona modes at cathode: (a) trichel streamers; (b) negative pulseless glow; (c) negative streamers. (Trinh and Jordan, 1968; Trinh, 1995.) Cathode: spherical protrusion ( $d = 0.8$  cm) on a sphere ( $D = 7$  cm); gap 19 cm; time exposure 1/4 sec.

accumulate in the region of the gap beyond  $S_0$ . Thus, as soon as the first electron avalanche has developed, there are two ion space charges in the gap.

The presence of these space charges increases the field near the cathode but it reduces the field intensity at the anode end of the gap. The boundary surface of zero ionization activity is therefore displaced toward the cathode. The subsequent electron avalanche develops in a region of slightly higher field intensity but covers a shorter distance than its predecessor. The influence of the ion space charge is such that it actually conditions the development of the discharge at the highly stressed electrode, producing three modes of corona discharge with distinct electrical, physical, and visual characteristics (Fig. 4.83). These are, respectively, with increasing field intensity: Trichel streamer, negative pulseless glow, and negative streamer. An interpretation of the physical mechanism of different corona modes is given below.

**Trichel Streamer**

Figure 4.83a shows the visual aspect of the discharge; its current and light characteristics are shown in Fig. 4.84. The discharge develops along a narrow channel from the cathode and follows a regular pattern

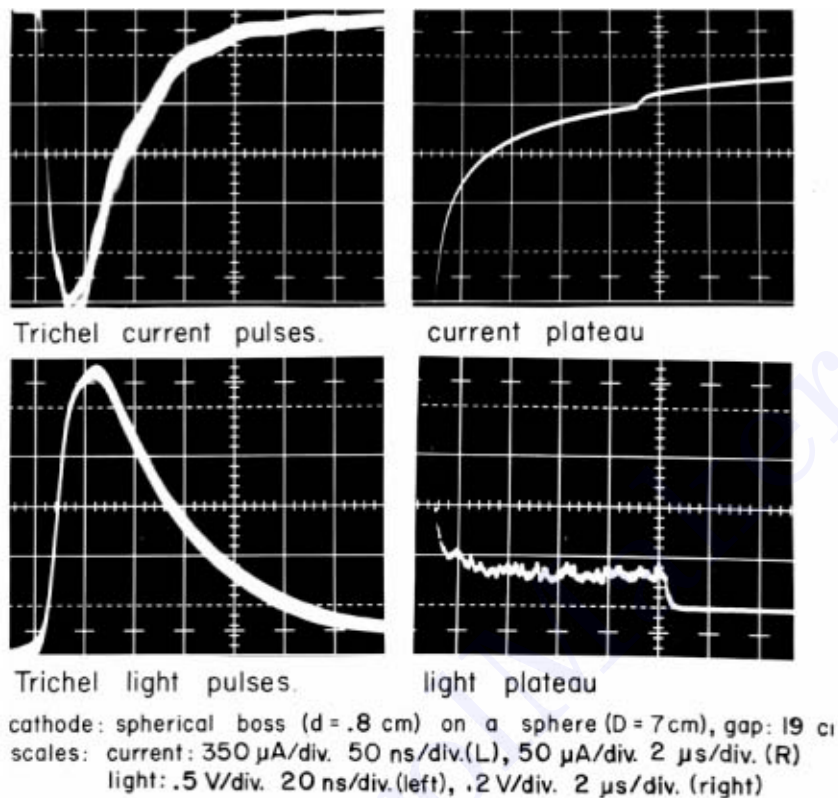


**FIGURE 4.84** Current and light characteristics of Trichel streamer. (Trinh and Jordan, 1968; Trinh, 1995.) Cathode: spherical protrusion ( $d = 0.8$  cm) on a sphere ( $D = 7$  cm); gap 19 cm. Scales: current  $350 \mu\text{A}/\text{div.}$ ,  $50 \text{ ns}/\text{div.}$  (left),  $50 \mu\text{A}/\text{div.}$ ,  $2 \mu\text{s}/\text{div.}$  (right). Light:  $0.5 \text{ V}/\text{div.}$ ,  $20 \text{ ns}/\text{div.}$  (left),  $0.2 \text{ V}/\text{div.}$ ,  $2 \mu\text{s}/\text{div.}$  (right).

in which the streamer is initiated, develops, and is suppressed; a short dead time follows before the cycle is repeated. The duration of an individual streamer is very short, a few tens of nanoseconds, while the dead time varies from a few microseconds to a few milliseconds, or even longer. The resulting discharge current consists of regular negative pulses of small amplitude and short duration, succeeding one another at the rate of a few thousand pulses per second. A typical Trichel current pulse is shown in Fig. 4.84a where, it should be noted, the waveshape is somewhat influenced by the time constant of the measuring circuit. The discharge duration may be significantly shorter, as depicted by the light pulse shown in Fig. 4.84b.

The development of Trichel streamers cannot be explained without taking account of the active roles of the ion space charges and the applied field. The streamer is initiated from the cathode by a free electron. If the corona onset conditions are met, the secondary emissions are sufficient to trigger new electron avalanches from the cathode and maintain the discharge activity. During the streamer development, several generations of electron avalanches are initiated from the cathode and propagate along the streamer channel. The avalanche process also produces two ion space charges in the gap, which moves the boundary surface  $S_0$  closer to the cathode. The positive ion cloud thus finds itself compressed at the cathode and, in addition, is partially neutralized at the cathode and by the negative ions produced in subsequent avalanches. This results in a net negative ion space charge, which eventually reduces the local field intensity at the cathode below the onset field and suppresses the discharge. The dead time is a period during which, the remaining ion space charges are dispersed by the applied field. A new streamer will develop when the space charges in the immediate surrounding of the cathode have been cleared to a sufficient extent.

This mechanism depends on a very active electron attachment process to suppress the ionization activity within a few tens of nanoseconds following the beginning of the discharge. The streamer repetition rate is essentially a function of the removal rate of ion space charges by the applied field, and generally shows a linear dependence on the applied voltage. However, at high fields a reduction in the pulse repetition rate may be observed, which corresponds to the transition to a new corona mode.

#### **Negative Pulseless Glow**

This corona mode is characterized by a pulseless discharge current. The discharge itself is particularly stable, as indicated by the well-defined visual aspect of the discharge (Fig. 4.83b) which shows the basic characteristics of a miniature glow discharge. Starting from the cathode, a cathode dark space can be distinguished, followed by a negative glow region, a Faraday dark space and, finally, a positive column of conical shape. As with low-pressure glow discharges, these features of the pulseless glow discharge result from very stable conditions of electron emission from the cathode by ionic bombardment. The electrons, emitted with very low kinetic energy, are first propelled through the cathode dark space where they acquire sufficient energy to ionize the gas, and intensive ionization occurs at the negative glow region. At the end of the negative glow region, the electrons lose most of their kinetic energy and are again accelerated across the Faraday dark space before they can ionize the gas atoms in the positive column. The conical shape of the positive column is attributed to the diffusion of the free electrons in the low-field region.

These stable discharge conditions may be explained by the greater efficiency of the applied field in removing the ion space charges at higher field intensities. Negative ion space charges cannot build up sufficiently close to the cathode to effectively reduce the cathode field and suppress the ionization activities there. This interpretation of the discharge mechanism is further supported by the existence of a plateau in the Trichel streamer current and light pulses (Fig. 4.84) which indicate that an equilibrium exists for a short time between the removal and the creation of the negative ion space charge. It has been shown (Trinh et al., 1970) that the transition from the Trichel streamer mode to the negative pulseless glow corresponds to an indefinite prolongation of one such current plateau.

#### **Negative Streamer**

If the applied voltage is increased still further, negative streamers may be observed, as illustrated in Fig. 4.83c. The discharge possesses essentially the same characteristics observed in the negative pulseless glow discharge but here the positive column of the glow discharge is constricted to form the streamer channel, which extends farther into the gap. The glow discharge characteristics observed at the cathode imply that this corona mode also depends largely on electron emissions from the cathode by ionic bombardment, while the formation of a streamer channel characterized by intensive ionization denotes an even more effective space charge removal action by the applied field. The streamer channel is fairly stable. It projects from the cathode into the gap and back again, giving rise to a pulsating fluctuation of relatively low frequency in the discharge current.

#### **Positive Corona Modes**

When the highly stressed electrode is of positive polarity, the electron avalanche is initiated at a point on the boundary surface  $S_0$  of zero net ionization and develops toward the anode in a continuously increasing field (Fig. 4.85). As a result, the highest ionization activity is observed at the anode. Here again, due to the lower mobility of the ions, a positive ion space charge is left behind along the development path of the avalanche. However, because of the high field intensity at the anode, few electron attachments occur and the majority of free electrons created are neutralized at the anode. Negative ions are formed mainly in the low-field region farther in the gap. The following discharge behavior may be observed (Trinh and Jordan, 1968; Trinh, 1995):

- The incoming free electrons are highly energetic and cannot be immediately absorbed by the anode. As a result, they tend to spread over the anode surface where they lose their energy through ionization of the gas particles, until they are neutralized at the anode, thus contributing to the development of the discharge over the anode surface.

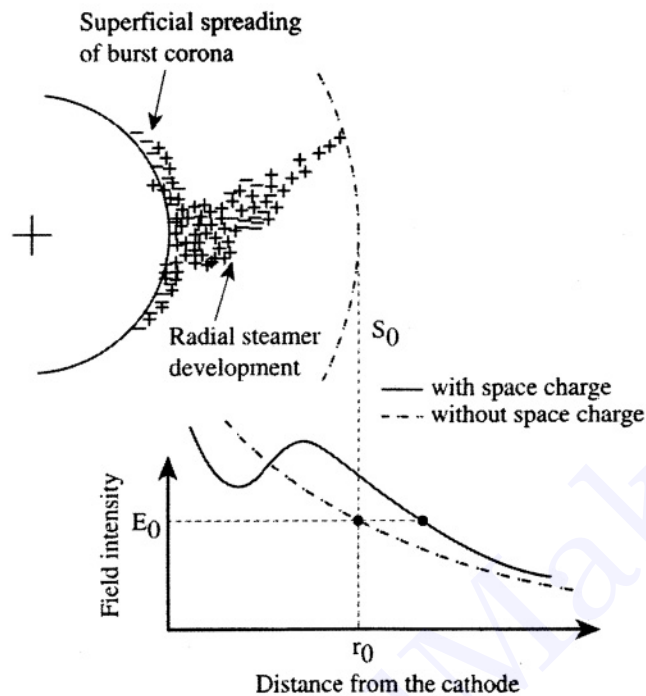


FIGURE 4.85 Development of an electron avalanche toward the anode. (Trinh, 1995.)

- Since the positive ions are concentrated immediately next to the anode surface, they may produce a field enhancement in the gap that attracts secondary electron avalanches and promotes the radial propagation of the discharge into the gap along a streamer channel. During streamer discharge, the ionization activity is observed to extend considerably into the low-field region of the gap via the formation of corona globules, which propagate owing to the action of the electric field generated by their own positive ion space charge. Dawson (1965) has shown that if a corona globule containing  $10^8$  positive ions within a spherical volume of  $3 \cdot 10^{-3}$  cm in radius is produced, the ion space charge field is such that it attracts sufficient new electron avalanches to create a new corona globule a short distance away. In the meantime, the initial corona globule is neutralized, causing the corona globule to effectively move ahead toward the cathode.

The presence of ion space charges of both polarities in the anode region greatly affects the local distribution of the field, and, consequently, the development of corona discharges at the anode. Four different corona discharge modes having distinct electrical, physical, and visual characteristics can be observed at a highly stressed anode, prior to flashover of the gap. These are, respectively, with increasing field intensity (Fig. 4.86): burst corona, onset streamers, positive-glow, and breakdown streamers. An interpretation of the physical mechanisms leading to the development of these corona modes is given below.

#### **Burst Corona**

This corona mode appears as a thin luminous sheath adhering closely to the anode surface (Fig. 4.86a). The discharge results from the spread of ionization activities at the anode surface, which allows the high-energy incoming electrons to lose their energy prior to neutralization at the anode. During this process, a number of positive ions are created in a small area over the anode which builds up a local positive space charge and suppresses the discharge. The spread of free electrons then moves to another part of the anode. The resulting discharge current consists of very small positive pulses (Fig. 4.87a), each corresponding to the ionization spreading over a small area at the anode and then being suppressed by the positive ion space charge produced.

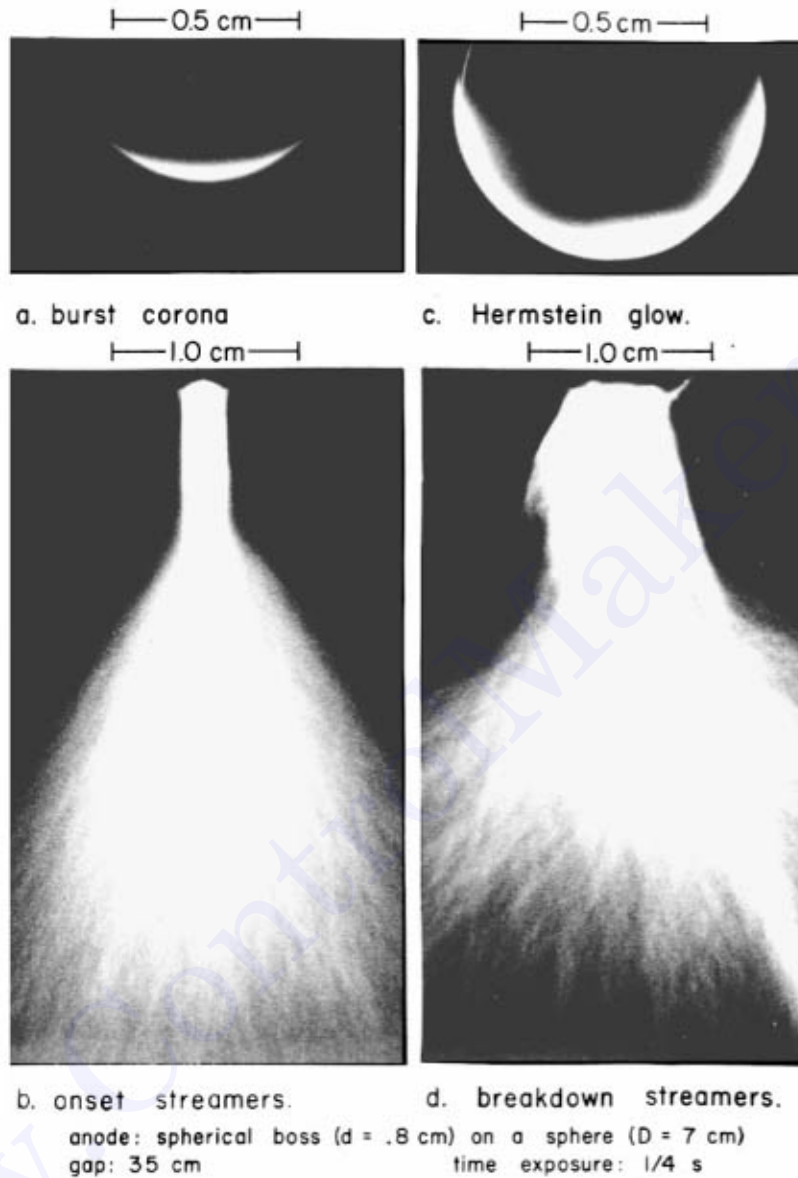


**FIGURE 4.86** Corona modes at anode: (a) burst corona, (b) onset streamers; (c) Hermstein anode glow corona, and (d) breakdown streamers. (Trinh and Jordan, 1968; Trinh, 1995.) Anode spherical protrusion ( $d = 0.8 \text{ cm}$ ) on a sphere ( $D = 7 \text{ cm}$ ); gap 35 cm; time exposure 1/4 sec.

#### **Onset Streamer**

The positive ion space charge formed adjacent to the anode surface causes a field enhancement in its immediate vicinity, which attracts subsequent electron avalanches and favors the radial development of onset streamers. This discharge mode is highly effective and the streamers are observed to extend farther into the low-field region of the gap along numerous filamentary channels, all originating from a common stem projecting from the anode (Fig. 4.86b). During this development of the streamers, a considerable number of positive ions are formed in the low-field region. As a result of the cumulative effect of the successive electron avalanches and the absorption at the anode of the free electrons created in the discharge, a net residual positive ion space charge forms in front of the anode. The local gradient at the

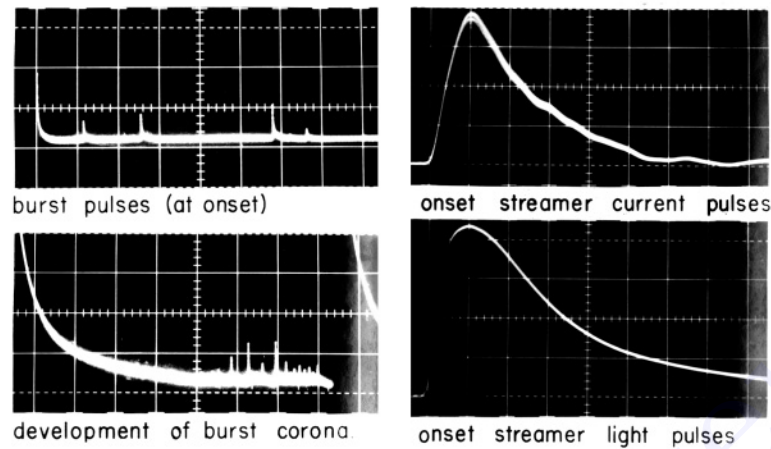


**FIGURE 4.87** (a) Burst corona current pulse. Scales: 5 mA/div., 0.2 ms/div. (Trinh and Jordan, 1968; Trinh, 1995). (b) Development of burst corona following a streamer discharge. Scales: 5 mA/div., 0.2 ms/div. (c) Current characteristics of onset streamers. Scales: 7 mA/div., 50 ns/div. (d) Light characteristics of onset streamers. Scales: 1 V/div., 20 ns/div.

anode then drops below the critical value for ionization and suppresses the streamer discharge. A dead time is consequently required for the applied field to remove the ion space charge and restore the proper conditions for the development of a new streamer. The discharge develops in a pulsating mode, producing a positive current pulse of short duration, high amplitude, and relatively low repetition rate due to the large number of ions created in a single streamer (Figs. 4.87c and d).

It has been observed that these first two discharge modes develop in parallel over a small range of voltages following corona onset. As the voltage is increased, it rapidly becomes more effective in removing the ion space charge in the immediate vicinity of the electrode surface, thus promoting the lateral spread of burst corona at the anode. In fact, burst corona can be triggered just a few microseconds after suppression of the streamer (Fig. 4.87b). This behavior can be explained by the rapid clearing of the positive ion space charge at the anode region, while the incoming negative ions encounter a high enough gradient to shed their electrons and sustain the ionization activity over the anode surface in the form of burst corona. The latter will continue to develop until it is again suppressed by its own positive space charge.

As the voltage is raised even higher, the burst corona is further enhanced by a more effective space charge removal action of the field at the anode. During the development of the burst corona, positive ions are created and rapidly pushed away from the anode. The accumulation of positive ions in front of the anode results in the formation of a stable positive ion-space charge that prevents the radial development of the discharge into the gap. Consequently, the burst corona develops more readily, at the expense of the onset streamer, until the latter is completely suppressed. A new mode, the positive-glow discharge, is then established at the anode.

#### **Positive Glow**

A photograph of a positive glow discharge developing at a spherical protrusion is presented in Fig. 4.86. This discharge is due to the development of the ionization activity over the anode surface, which forms a thin luminous layer immediately adjacent to the anode surface, where intense ionization activity takes place. The discharge current consists of a direct current superimposed by a small pulsating component with a high repetition rate, in the hundreds of kilohertz range. A photomultiplier study of the light emitted reveals that the uniform ionizing sheath projects from a central region and back again, continuously, following the burst of ionization activity at the anode, which gives rise to the pulsating current component.

The development of the positive glow discharge may be interpreted as resulting from a particular combination of removal and creation of positive ions in the gap. The field is high enough for the positive ion space charge to be rapidly removed from the anode, thus promoting surface ionization activity. Meanwhile, the field intensity is not sufficient to allow radial development of the discharge and the formation of streamers. The main contribution of the negative ions is to supply the necessary triggering electrons to sustain ionization activity at the anode.

#### **Breakdown Streamer**

If the applied voltage is further increased, streamers are again observed and they eventually lead to breakdown of the gap. The development of breakdown streamers is preceded by local *streamer spots* of intense ionization activity which may be seen moving slowly over the anode surface. The development of streamer spots is not accompanied by any marked change in the current or the light signal. Only when the applied field becomes sufficiently high to rapidly clear the positive ion space charges from the anode region does radial development of the discharge become possible, resulting in breakdown streamers.

Positive breakdown streamers develop more and more intensively with higher applied voltage and eventually cause the gap to break down. The discharge is essentially the same as the onset streamer type but can extend much farther into the gap. The streamer current is more intense and may occur at a higher repetition rate. A streamer crossing the gap does not necessarily result in gap breakdown, which proves that the filamentary region of the streamer is not fully conducting.

#### **AC Corona**

When alternating voltage is used, the gradient at the highly stressed electrode varies continuously, both in intensity and in polarity. Different corona modes can be observed in the same cycle of the applied voltage. Figure 4.88 illustrates the development of different corona modes at a spherical protrusion as a function of the applied voltage. The corona modes can be readily identified by the discharge current. The following observations can be made:

- For short gaps, the ion space charges created in one half-cycle are absorbed by the electrodes in the same half-cycle. The same corona modes that develop near onset voltages can be observed, namely: negative Trichel streamers, positive onset streamers, and burst corona.
- For long gaps, the ion space charges created in one half-cycle are not completely absorbed by the electrodes. The residual space charges are drawn back to the region of high field intensity in the following half-cycle and can influence discharge development. Onset streamers are suppressed in favor of the positive glow discharge. The following corona modes can be distinguished: negative Trichel streamers, negative glow discharge, positive glow discharge, and positive breakdown streamers.
- Negative streamers are not observed under AC voltage, owing to the fact that their onset gradient is higher than the breakdown voltage that occurs during the positive half-cycle.

### **Main Effects of Corona Discharges on Overhead Lines (Trinh, 1995)**

Impact of corona discharges on the design of high-voltage lines has been recognized since the early days of electric power transmission when the corona losses were the limiting factor. Even today, corona losses remain critical for HV lines below 300 kV. With the development of EHV lines operating at voltages between 300 and 800 kV, electromagnetic interferences become the designing parameters. For UHV lines operating at voltages above 800 kV, the audible noise appears to gain in importance over the other two parameters. The physical mechanisms of these effects — corona losses, electromagnetic interference, and audible noise — will be given and their current evaluation methods discussed below.

#### **Corona Losses**

The movement of ions of both polarities generated by corona discharges, and subjected to the applied field around the line conductors, is the main source of energy loss. For AC lines, the movement of the

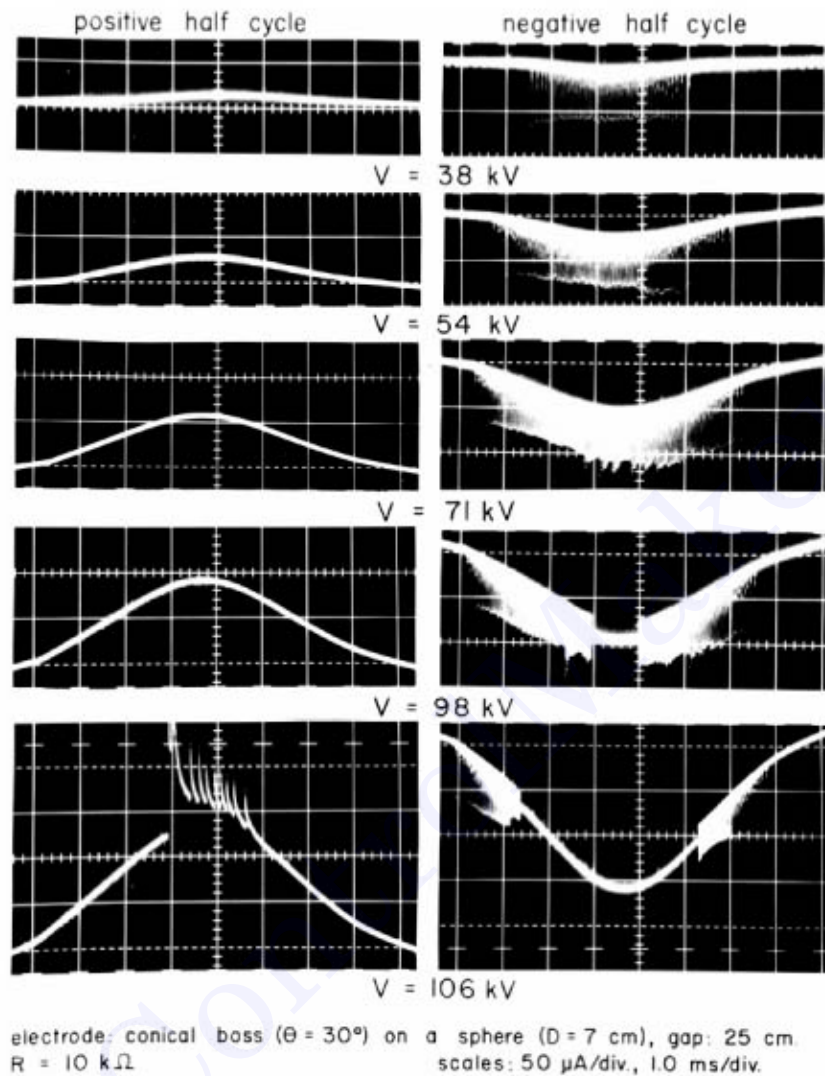


**FIGURE 4.88** Corona modes under AC voltage. (Trinh and Jordan, 1968; Trinh, 1995.) Electrode: conical protrusion ( $\theta = 30^\circ$ ) on a sphere ( $D = 7\text{ cm}$ ); gap 25 cm;  $R = 10\text{ k}\Omega$ ; Scales:  $50\ \mu\text{A}/\text{div.}$ ,  $1.0\ \text{ms}/\text{div.}$

ion space charges is limited to the immediate vicinity of the line conductors, corresponding to their maximum displacement during one half-cycle, typically a few tens of centimeters, before the voltage changes polarity and reverses the ionic movement. For DC lines, the ion displacement covers the whole distance separating the line conductors, and between the conductors and the ground.

Corona losses are generally described in terms of the energy losses per kilometer of the line. They are generally negligible under fair-weather conditions but can reach values of several hundreds of kilowatts per kilometer of line during foul weather. Direct measurement of corona losses is relatively complex, but foul-weather losses can be readily evaluated in *test cages* under artificial rain conditions, which yield the highest energy loss. The results are expressed in terms of the *generated loss*  $W$ , a characteristic of the conductor to produce corona losses under given operating conditions.

### Electromagnetic Interference

Electromagnetic interference is associated with streamer discharges that inject current pulses into the conductor. These steep-front, short-duration pulses have a high harmonic content, reaching the tens of

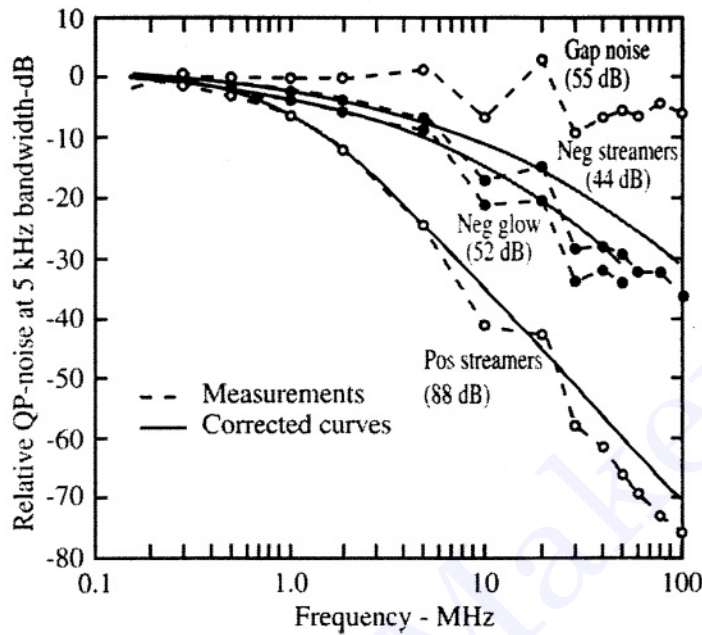


FIGURE 4.89 Relative frequency spectra for different noise types. (Trinh, 1995; Juette, 1972.)

megahertz range, as illustrated in Fig. 4.89, which shows the typical frequency spectra associated with various streamer modes (Juette, 1972). A tremendous research effort was devoted to the subject during the years 1950–80 in an effort to evaluate the electromagnetic interference from HV lines. The most comprehensive contributions were made by Moreau and Gary (1972) of Électricité de France, who introduced the concept of the *excitation function*,  $\Gamma(\omega)$ , which characterizes the ability of a line conductor to generate electromagnetic interference under given operating conditions.

Consider first the case of a single-phase line, where the contribution to the electromagnetic interference at the measuring frequency  $\omega$ , from corona discharges developing at a section  $dx$  of the conductor is

$$i_0(\omega)dx = C \Gamma(\omega)dx \tag{4.135}$$

where  $C$  is the capacitance per unit length of the line conductor to ground.

Upon injection, the discharge current pulse splits itself in two identical current pulses of half-amplitude propagating in opposite directions away from the discharge site. At a point of observation located at a distance  $x$  along the line from the discharge site, the noise current is distorted according to

$$i(\omega, x)dx = i_0(\omega)\exp(-\gamma x)dx \tag{4.136}$$

where  $\gamma$  represents the propagation constant, which can be approximated by its real component  $\alpha$ .

The total noise current circulating in the line conductor is the sum of all contributions from the corona discharges along the conductor and is given by

$$I(\omega) = \sqrt{\int_{-\infty}^{\infty} [i(\omega, x)]^2 dx} = \frac{i_0(\omega)}{\sqrt{\alpha}} \tag{4.137}$$

Circulation of the noise current in the line conductor effectively generates an electromagnetic interference field around the conductors, which is readily picked up by any radio or TV receiver located in the vicinity of the HV line. The current practices characterize the interference field in terms of its electric component,  $E(\omega)$ , expressed in decibels (dB) above a reference level of  $1 \mu\text{V/m}$ . Evaluation of the electromagnetic interference is usually made by first calculating the magnetic interference field  $H(\omega)$  at the measuring point

$$H(\omega) = \sum_j \frac{1}{2\pi r_j} I_j(\omega) \mathbf{a}_r. \quad (4.138)$$

The summation was made with respect to the number of phase conductors of the lines and their images with respect to the magnetic ground. The electric interference field can next be related to the magnetic interference field according to

$$E(\omega) = \sqrt{\frac{\mu_0}{\epsilon_0}} H(\omega). \quad (4.139)$$

For a multi-phase line, because of the high-frequency nature of the noise current, the calculation of the interference field must take account of the mutual coupling among the conductors, which further complicates the process (Gary, 1972; Moreau et al., 1972). Modal analysis provides a convenient means of evaluating the noise currents on the line conductors. In this approach, the noise currents are first transposed into their modal components, which propagate without distortion along the line conductors at their own velocity according to the relation

$$[i_0(\omega) dx] = [M] [j_0(\omega) dx]. \quad (4.140)$$

Consequently,

$$[j_0(\omega) dx] = [M]^{-1} [i_0(\omega) dx] \quad (4.141)$$

where  $[M]$  is the modal transposition matrix and  $j_0(\omega)$  are the modal components of the injected noise current. The modal current at the measuring point located at a distance  $x$  from the injection point is:

$$j(\omega, x) dx = j_0(\omega) \exp(-\alpha x) dx, \quad (4.142)$$

and the modal current component at the measuring point is

$$J(\omega) = \sqrt{\int_{-\infty}^{\infty} [j(\omega, x)]^2 dx} = \frac{j_0(\omega)}{\sqrt{\alpha}}, \quad (4.143)$$

or, in a general way

$$[J(\omega)] = \frac{1}{\sqrt{\alpha}} [j_0(\omega)] = \frac{1}{\sqrt{\alpha}} [M]^{-1} [i_0(\omega)]. \quad (4.144)$$

Finally, the line current can be obtained from

$$[I(\omega)] = [M][J(\omega)] \quad (4.145)$$

The magnetic and electric fields produced by the noise currents in the line conductors can then be evaluated using Eqs. (4.138) and (4.139). Gary and Moreau (1972) obtained good agreement between calculated and experimental results with the symmetrical modes of Clarke for the modal transposition.

$$[M] = \begin{bmatrix} 1/\sqrt{6} & 1/2 & 1/\sqrt{3} \\ -2/\sqrt{6} & 0 & 1/\sqrt{3} \\ 1/\sqrt{6} & -1/2 & 1/\sqrt{3} \end{bmatrix}$$

The attenuation coefficients at 0.5 MHz are 11.1, 54, and 342 Np/m for the modal currents, and the magnetic ground was assumed to be located at a depth equal to the penetration depth of the magnetic field as defined by

$$P = \sqrt{\frac{2\rho}{\mu_0\omega}} \quad (4.146)$$

For a typical soil resistivity of 100 Ohm-m and a measuring frequency of 0.5 MHz, the depth of the magnetic ground is equal to 7.11 m.

#### TV Interference

The frequency spectrum of corona discharges has cut-off frequencies around a few tens of megahertz. As a result, the interference levels at the TV frequencies are very much attenuated. In fact, gap discharges, which generate sharp current pulse with nanosecond risetimes, are the principal discharges that effectively interfere with TV reception. These discharges are produced by loose connections, a problem common on low-voltage distribution lines but rarely observed on high-voltage transmission lines. Another source of interference is related to reflections of TV signals at high-voltage line towers, producing ghost images. However, the problem is not related in any way to corona activities on the line conductors (Juette, 1972).

#### Audible Noise

The high temperature in the discharge channel produced by the streamer creates a corresponding increase in the local air pressure. Consequently, a pulsating sound wave is generated from the discharge site, propagates through the surrounding ambient air, and is perfectly audible in the immediate vicinity of the HV lines. The typical octave-band frequency spectra of line corona in Fig. 4.90 contains discrete components corresponding to the second and higher harmonics of the line voltage superimposed on a relatively broad-band noise, extending well into the ultrasonic range (Ianna et al., 1974). The octave band measurements in this figure show a sharp drop at frequencies over 20 kHz, due principally to the limited frequency response of the microphone and associated sound-level meter.

Similar to the case of electromagnetic interference, the ability of the line conductors to produce audible noise is characterized by the *generated acoustic power density A*, defined as the acoustic power produced per unit length of the line conductor under specific operating conditions. The acoustic power generated by corona discharges developing in a portion  $dx$  of the conductor is then

$$dA = A dx. \quad (4.147)$$

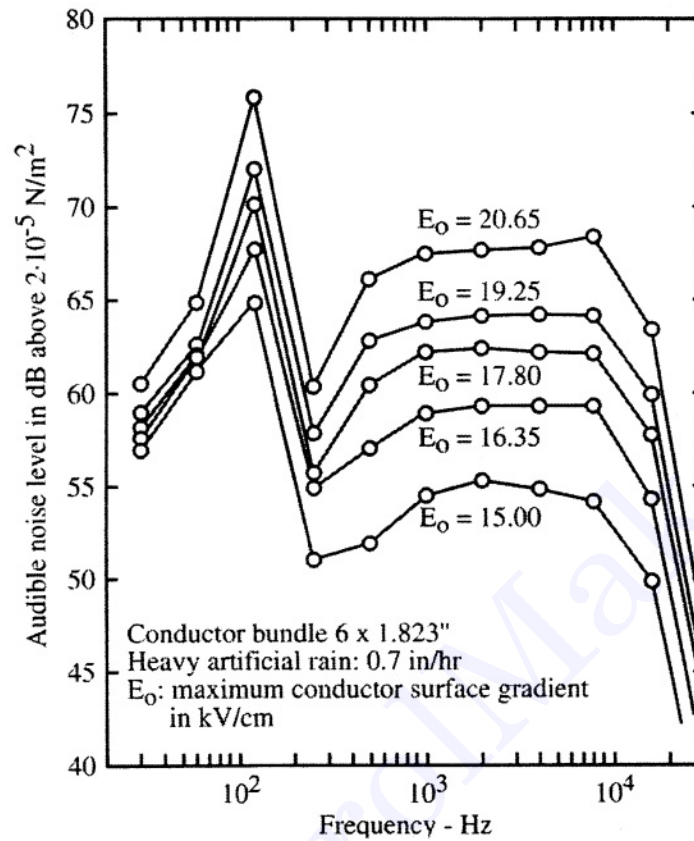


FIGURE 4.90 Octave-band frequency-spectrum of line corona audible noise at 10 m from the conductor. (Trinh, 1995; Trinh et al., 1977.)

Its contribution to the acoustic intensity at a measuring point located at a distance  $r$  from the discharge site is

$$dI = \frac{A}{4\pi r^2} dx. \tag{4.148}$$

The acoustic intensity at the measuring point is the sum of all contributions from corona discharge distributed along the conductor:

$$I(R) = 2A \int_{-\infty}^{\infty} \frac{1}{4\pi(R^2 + x^2)} dx = \frac{A}{2R} \tag{4.149}$$

where  $R$  is the distance from the measuring point to the conductor, and the integral is evaluated in terms of the longitudinal distance  $x$  along the conductor. Finally, the acoustic intensity at the measuring point is the sum of the contributions from the different phase conductors of the line

$$I(R) = \sum_j I_j(R). \tag{4.150}$$

TABLE 4.25 Hydro-Québec 735-kV Line

Distance between phase (m)	13.7	
Height of conductors (m)	19.8	
Number of sub-conductors	4	
Diameter of sub-conductor (cm)	3.05	
	<b>Center phase</b>	<b>Outer phase</b>
Electric field at the conductor surface (kVrms/cm)	19.79	18.46
Capacitance per unit length (pF/m)	10.57	
Generated loss W (W/m)	59.77	33.92
RI excitation function $\Gamma$ (dB above 1 $\mu\text{A}/\sqrt{\text{m}}$ )	43.52	39.59
Subconductor generated acoustic power density A (dBA above 1 $\mu\text{W}/\text{m}$ )	3.28	-0.24

The sound pressure, usually expressed in terms of decibel (dBA) above a reference level of  $2 \times 10^{-5} \text{ N/m}^2$ , is

$$p(r) = \sqrt{\rho_0 C I} \quad (4.151)$$

### Example of Calculation

It is obvious from the preceding sections that the effects of corona discharges on HV lines — the corona losses, the electromagnetic interferences, and audible noise — can be readily evaluated from the generated loss W, the excitation function  $\Gamma(\omega)$ , and the generated acoustic power density A of the conductor. The latter parameters are characteristics of the bundle conductor and are usually derived from tests in a test cage or on experimental line. An example calculation of the corona performance of a HV line is given below for the case of the Hydro-Québec's 735-kV lines under conditions of heavy rain. The line parameters are given in Table 4.25, together with the various corona-generated parameters taken from Trinh et al. (1977). The calculation of the radio interference and audible noise levels will be made for a lateral distance of 15 m from the outer phase, i.e., at the limit of the right of way of the line.

**Corona losses:** The corona losses are the sum of the losses generated at the three phases of the line, which amount to 127.63 kW/km.

**Radio interference:** The calculation of the radio interference requires that the noise current be first transformed into its modal components. Consider a noise current of unit excitation function  $\Gamma_a(\omega) = 1.0 \mu\text{A}/\sqrt{\text{m}}$  circulating in phase A of the line. Because of the capacitive coupling, it induces currents to the other two phases of the line as well. For Hydro-Québec's 735-kV line, the capacitance matrix is

$$C = \begin{bmatrix} 11.204 & -2.241 & -0.73 \\ -2.241 & 11.605 & -2.241 \\ -0.73 & -2.241 & 11.204 \end{bmatrix} \text{ pF/m,}$$

and the noise current in phase A and its induced currents to phases B and C are

$$i_a(\omega) = \begin{bmatrix} 11.204 \\ -2.241 \\ -0.73 \end{bmatrix} \mu\text{A}.$$

The modal transformation using Eqs. (4.141–4.144) gives the following modal noise currents at the measuring point, taking into account of the different attenuations of the modal currents.

$$J_a(\omega) = \begin{bmatrix} 16.472 & 10.321 & 2.31 \\ -30.497 & 0 & 1.998 \\ 16.472 & -10.321 & 2.31 \end{bmatrix} \mu A$$

These modal currents, once transformed back to the current mode, Eq. (4.145), give the modal components of the noise currents flowing in the line conductors at the measuring point as related to the noise current injected to phase A.

$$I_a(\omega) = \begin{bmatrix} 6.725 & 7.298 & 1.333 \\ -13.449 & 0 & 1.333 \\ 6.725 & -7.298 & 1.333 \end{bmatrix} \mu A$$

These currents can then be used to calculate the magnetic and electric interference field using Eqs. (4.138) and (4.139)

$$H_a(\omega) = \begin{bmatrix} 0.0124 & 0.0449 & 0.0239 \end{bmatrix} \mu A/m$$

$$E_a(\omega) = \begin{bmatrix} 4.674 & 16.938 & 9.017 \end{bmatrix} \mu V/m$$

The corresponding electric interference level is 25.911 dB above 1 μV/m.

The above electric interference field and interference level are obtained assuming a noise excitation function of 1.0 μA/√m. For the case of interest, the excitation function at phase A is 39.59 dB and the corresponding interference level is 64.98 dB. By repeating the same process for the noise currents injected in phases B and C, one obtains effectively three sets of magnetic and electric field components generated by the circulation of the noise currents on the line conductors.

$$E_b(\omega) = \begin{bmatrix} -8.653 & 0 & 7.80 \end{bmatrix} \mu V/m, \text{ and}$$

$$E_c(\omega) = \begin{bmatrix} 4.674 & -16.938 & 9.017 \end{bmatrix} \mu V/m$$

Their contributions to the noise level are, respectively, 64.26 dB and 64.98 dB, resulting in a total noise level of 69.53 dB at the measuring point. The measuring frequency is 0.5 MHz.

**Audible noise:** Calculation of the audible noise is straightforward, since each phase of the line can be considered as an independent noise source. Consider the audible noise generated from phase A. The subconductor generated acoustic power density is -0.24 dBA or 1.58 10<sup>-5</sup> μW/m for the bundle conductor. The acoustic intensity at 15 m from the outer phase of the line as given by Eq. (4.149) is 3.19 10<sup>-7</sup> W/m<sup>2</sup> and the noise level is 55.14 dBA above 2 10<sup>-5</sup> N/m<sup>2</sup>.

By repeating the process for the other two phases of the line, the contributions to the acoustic intensity at the measuring point from the phase B and C of the line are 2.64 10<sup>-7</sup> and 1.69 10<sup>-7</sup> W/m<sup>2</sup>, respectively, and the corresponding noise levels are 54.33 dBA and 52.38 dBA. The total noise level is 58.87 dBA.

## Impact on the Selection of Line Conductors

### Corona Performance of HV Lines

Corona performance is a general term used to characterize the three main effects of corona discharges developing on the line conductors and their related hardware, namely corona losses (CL), electromagnetic interference (RI), and audible noise (AN). All are sensitive to weather conditions, which dictate the corona

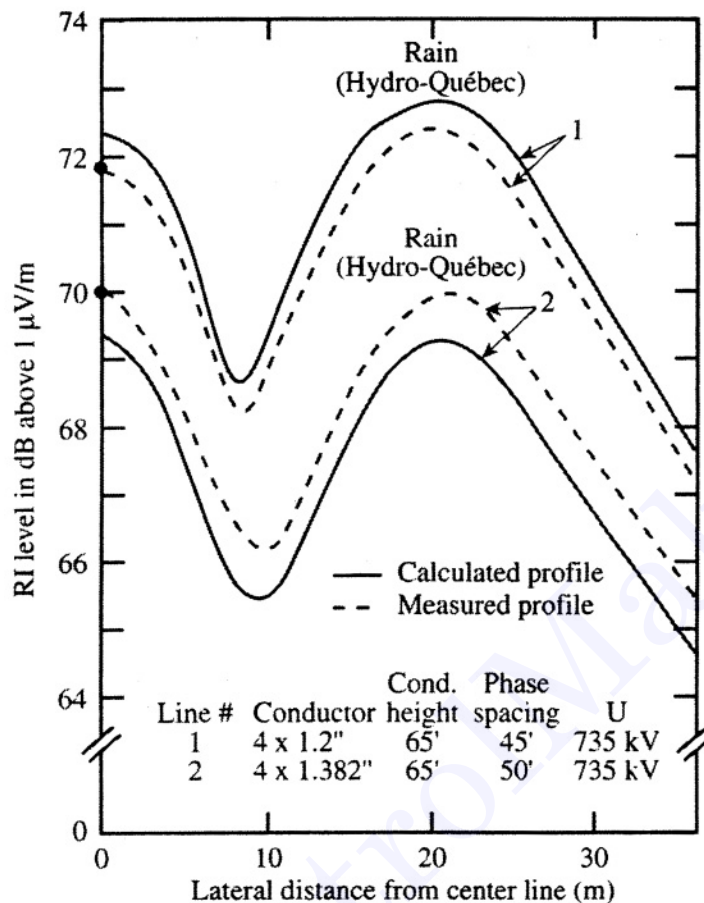


**FIGURE 4.91** Comparison of calculated and measured RI performances of Hydro-Québec 735-kV lines at 1 MHz and using natural modes. (Trinh, 1995; Trinh et al., 1977.)

activities. Corona losses can be described by a lump figure, which is equal to the total energy losses per kilometer of the line. Both the electromagnetic interference and the audible noise levels vary with the distance from the line and are best described by lateral profiles, which show the variations in the RI and AN level with the lateral distance from the line. Typical lateral profiles are presented in Figs. 4.91 and 4.92 for a number of HV lines under foul-weather conditions. For convenience, the interference and noise levels at the edge of the right-of-way, typically 15 m from the outside phases of the line, are generally used to quantify the interference and noise level.

The time variations in the corona performance of HV lines is best described in terms of a statistical distribution, which shows the proportion of time that the energy losses, the electromagnetic interference, and audible noise exceed their specified levels. Figure 4.93 illustrates typical corona performances of Hydro-Québec’s 735-kV lines as measured at the edge of the right-of-way. It can be seen that the RI and AN levels vary over wide ranges. In addition, the cumulative distribution curves show a typical inverted-S shape, indicating that the recorded data actually result from the combination of more than one population, usually associated with fair and foul weather conditions.

DC coronas are less noisy than AC coronas. In effect, although DC lines can become very lossy during foul weather, the radio interference and audible noises are significantly reduced. This behavior is related to the fact that water drops become elongated, remain stable, and produce glow corona modes rather than streamers in a DC field (Ianna et al., 1974).

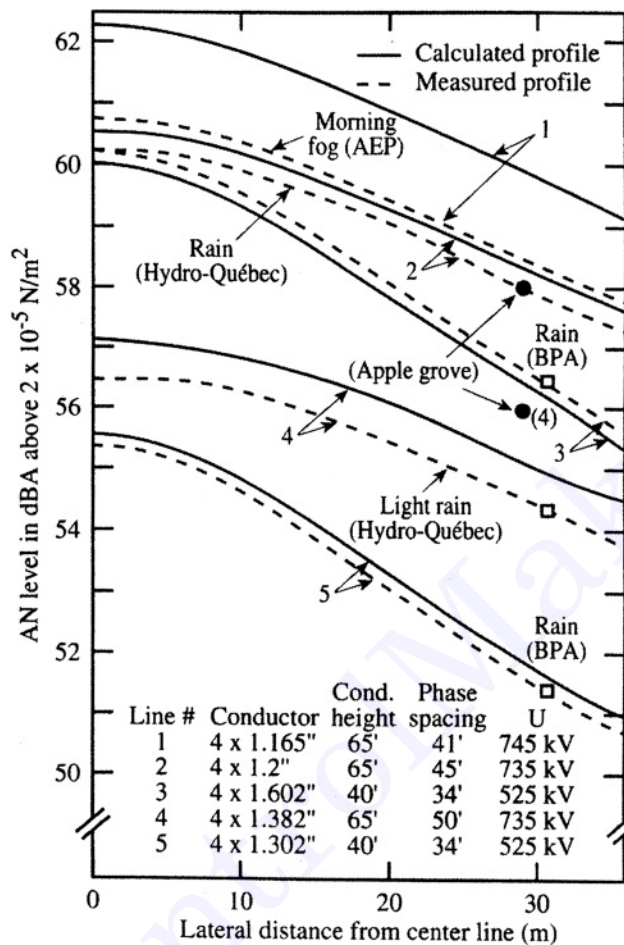


FIGURE 4.92 Comparison of calculated and measured AN performances of HV lines. (Trinh, 1995; Trinh et al., 1977.)

### Approach to Control the Corona Performance

The occurrence of corona discharges on line conductors is dictated essentially by the local field intensity, which, in turn, is greatly affected by the surface conditions, e.g., rugosity, water drops, snow and ice particles, etc. For a smooth cylindrical conductor, the corona onset field is well described by the Peek's experimental law

$$E_c = 30m\delta \left( 1 + \frac{0.301}{\sqrt{\delta a}} \right) \quad (\text{kVp/cm}) \quad (4.152)$$

where  $E_c$  is the corona onset field,  $a$  is the radius of the conductor, and  $m$  is an experimental factor to take account of the surface conditions. Typical values of  $m$  are 0.8–0.9 for a dry aged conductor, 0.5–0.7 for a conductor under foul weather conditions, and  $\delta$  is the relative air density factor.

The above corona onset condition emphasizes the great sensitivity of corona activities to the conductor surface condition and, hence, to changes in weather conditions. In effect, although the line voltage and the nominal conductor surface gradient remain constant, the surface condition factor varies continuously

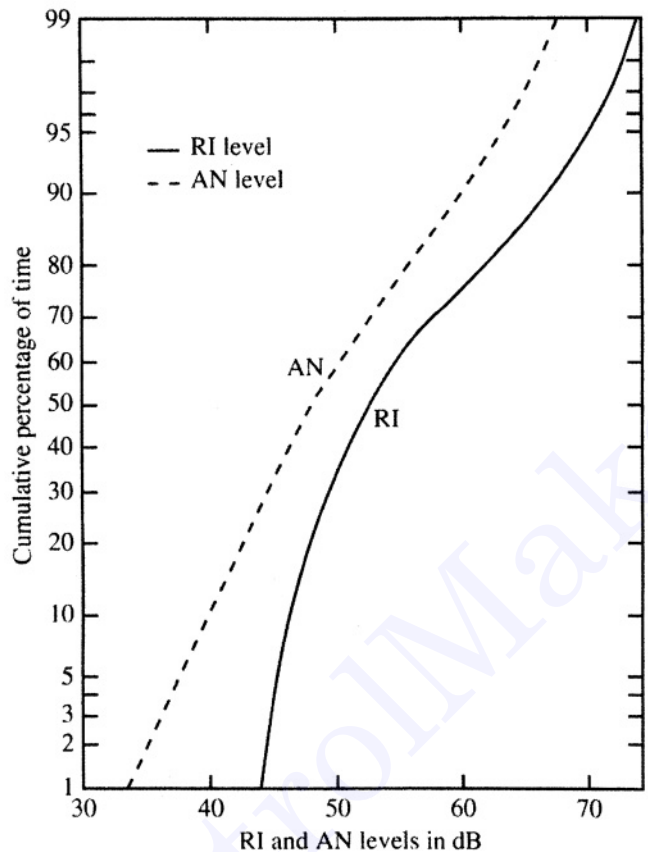


**FIGURE 4.93** Cumulative distribution of RI and AN levels measured at 15 m from the outer phases of Hydro-Québec 735-kV lines. (Trinh, 1995.)

due to the exposure of line conductors to atmospheric conditions. The changes are particularly pronounced during foul weather as a result of the numerous discharge sites associated with water drops, snow, and ice particles deposited on the conductor surface.

Adequate corona performance of HV lines is generally achieved by a proper control of the field intensity at the surface of the conductor. It can be well-illustrated by the simple case of a single-phase, single-conductor line for which the field intensity at the conductor surface is

$$E_0 = \frac{1}{\ln\left(\frac{2h}{a}\right)} \frac{U}{a} \leq E_c. \quad (4.153)$$

It can be seen that the field intensity at the conductor surface is inversely proportional to its radius and, to a lesser extent, to the height of the conductor above ground. By properly dimensioning the conductor, the field intensity at its surface can be kept below the fair-weather corona-onset field for an adequate control of the corona activities and their undesirable effects.

With the single-conductor configuration, the size required for the conductor to be corona-free under fair weather conditions is roughly proportional to the line voltage, and consequently will reach unrealistic values when the latter exceeds some 400 kV. Introduced in 1910 by Whitehead to increase the transmission capability of overhead lines (1910), the concept of *bundled conductors* quickly revealed itself as an effective means of controlling the field intensity at the conductor surface, and hence, the line corona activities.

**TABLE 4.26** Comparison of Single and Bundled Conductors Performances

Line voltage (kV)	400	735	1100
Distance between phases (m)	12	13.7	17
Number of subconductors	2	4	8
Bundle diameter (cm)	45	65	84
<b>Conductor diameter (cm)</b>	<b>3.2</b>	<b>3.05</b>	<b>3.2</b>
Corona onset gradient, $m = 0.85$ , (kVrms/cm)	22.32	22.04	22.32
Maximum surface gradient (kVrms/cm)	16.3	19.79	17.3
<b>Single conductor diameter of the same gradient (cm)</b>	<b>4.7</b>	<b>8.5</b>	<b>13.8</b>
Transmission capability (GW)	0.5	2.0	4.9
<b>Single conductor diameter of the same transmission capability (cm)</b>	<b>8.5</b>	<b>22</b>	<b>64</b>

This is well-illustrated by the results in Table 4.26, which compare the single conductor design required to match the bundle performances in terms of power transmission capabilities, and the maximum conductor surface gradient for different line voltages. Bundled conductors are now used extensively in EHV lines rated 315 kV and higher; as a matter of fact, HV lines as we know them today would not exist without the introduction of conductor bundles.

### Selection of Line Conductors

Even with the use of bundled conductors, it is not economically justifiable to design line conductors that would be corona-free under all weather conditions. The selection of line conductors is therefore made in terms of them being relatively corona-free under fair weather. While corona activities are tolerated under foul weather, their effects are controlled to acceptable levels at the edge of the rights-of-way of the line. For AC lines, the design levels of 70 dB for the radio interference and 60 dBA for the audible noise at the edge of the right-of-way are often used (Trinh et al., 1974). These levels may be reached during periods of foul weather, and for a specified annual proportion of time, typically 15–20%, depending on the local distribution of the weather pattern. The design process involves extensive field calculations and experimental testing to determine the number and size of the line conductors required to minimize the undesirable effects of corona discharges. Current practices in dimensioning HV line conductors usually involve two stages of selection according to their worst-case and long-term corona performances.

#### Worst-Case Performance

Several conductor configurations (number, spacing, and diameter of the subconductors) are selected with respect to their worst-case performances which, for AC lines, corresponds to foul-weather conditions, in particular heavy rain. Evaluation of the conductor worst-case performance is best done in *test cages* under artificial heavy rain conditions (Trinh and Maruvada, 1977). Test cages of square section, typically 3 m × 3 m, and a few tens of meters long, are adequate for evaluating full-size conductor bundles located along its central axis, for lines up to the 1500-kV class. The advantages of this experimental setup are the relatively modest test voltage required to reproduce the same field distribution on real-size bundled conductors, and the possibility of artificially producing the heavy rain conditions. The worst-case performance of various bundled conductors can then be determined over a wide range of surface gradients.

Under DC voltage, the worst-case corona performance is not directly related to foul-weather conditions. Although heavy rain was found to produce the highest losses, both the electromagnetic interference and the audible noise levels decrease under rain conditions. This behavior is related to the fact that under DC field conditions, the water droplets have an optimum shape, favorable to the development of stable glow-corona modes (Ianna et al., 1974). For this reason, test cage is less effective in evaluating the worst-case DC performance of bundled conductors.

A significant amount of data was gathered in cage tests at IREQ during the 1970s and provided the database for the development of a method to predict the worst-case performance of bundled conductors for AC voltage (Trinh and Maruvada, 1977). The results presented in Figs. 4.91 and 4.92, which compare the calculated and measured lateral RI and AN profiles of a number of HV lines, illustrate the good concordance of this approach. Commercial softwares exist that evaluate the worst-case performance of

HV line conductors using available experimental data obtained in cage tests under conditions of artificial heavy rain, making it possible to avoid undergoing tedious and expensive tests to help select the best configurations for line conductors for a given rating of the line.

#### **Long-Term Corona Performance**

Because of their wide range of variation in different weather conditions, representative corona performances of HV line are best evaluated in their natural environment. Test lines are generally used in this study which involves energizing the conductors for a sufficiently long period, usually one year to cover most of the weather conditions, and recording their corona performances together with the weather conditions. The higher cost of the long-term corona performance study usually limits its application to a small number of conductor configurations selected from their worst-case performance.

It should be noted that best results for the long-term corona performance evaluated on test lines are obtained when the weather pattern at the test site is similar to that existing along the actual HV line. A direct transposition of the results is then possible. If this condition is not met, some interpretation of the experimental data is needed. This is done by first decomposing the recorded long-term data into two groups, corresponding to the fair and foul weather conditions, then recombining these data according to the local weather pattern to predict the long-term corona performance along the line.

### **Conclusions**

This section on transmission systems has reviewed the physics of corona discharges and discussed their impact on the design of high-voltage lines, specifically in the selection of the line conductors. The following conclusions can be drawn.

- Corona discharges can develop in different modes, depending on the equilibrium state existing under a given test condition, between the buildup and removal of ion space charges from the immediate vicinity of the highly stressed electrode. Three different corona modes, Trichel streamer, negative glow, and negative streamer, can be observed at the cathode with increasing applied field intensities. With positive polarity, four different corona modes are observed, namely burst corona, onset streamers, positive glow, and breakdown streamers.
- While all corona modes produce energy losses, the streamer discharges also generate electromagnetic interference and audible noise in the immediate vicinity of HV lines. These parameters are currently used to evaluate the corona performance of conductor bundles and to predict the energy losses and environmental impact of HV lines prior to their installation.
- Adequate control of line corona is obtained by controlling the surface gradient at the line conductors. The introduction of bundled conductors in 1910 has greatly influenced the development of HV lines to today's EHV voltages.
- Commercial softwares are available to select the bundle configuration: number and size of the subconductors, with respect to corona performances, which can be verified in test cages and lines in the early stage of new HV-line projects.

### **References**

- Bateman, L.A., Haywood, R.W., and Brooks, R.F., Nelson River DC Transmission Project, *IEEE Trans.*, PAS-88, 688, 1969.
- Bortnik, I.M., Belyakov, N.N., Djakov, A.F., Horoshev, M.I., Ilynichin, V.V., Kartashev, I.I., Nikitin, O.A., Rashkes, V.S., Tikhodeyev, N.N., and Volkova, O.V., *1200 kV Transmission Line in the USSR: The First Results of Operation*, in *CIGRE Report No. 38-09*, Paris, August 1988.
- Dawson, G. A., A model for streamer propagation, *Zeitschrift für Physik*, 183, 159, 1965.
- Gary, C. H., The theory of the excitation function: A demonstration of its physical meaning, *IEEE Trans.*, PAS-91, 305, 1972.

- Ianna, F., Wilson, G.L., and Bosak, D.J., Spectral characteristics of acoustic noise from metallic protrusion and water droplets in high electric fields, *IEEE Trans.*, PAS-93, 1787, 1974.
- Juette, G. W., Evaluation of television interference from high-voltage transmission lines, *IEEE Trans.*, PAS-91, 865, 1972.
- Krishnayya, P.C.S., Lambeth, P.J., Maruvada, P.S., Trinh, N.G., and Desilets, G., *An Evaluation of the R&D Requirements for developing HVDC Converter Stations for Voltages above  $\pm 600$  kV*, in *CIGRE Report No. 14-07*, Paris, August 1988.
- Lacroix, R. and Charbonneau, H., Radio Interference from the first 735-kV line of Hydro-Quebec, *IEEE Trans.*, PAS-87, 932, 1968.
- Loeb, L.B., *Electrical Corona*, University of California Press, 1965.
- Moreau, M. R. and Gary, C. H., Predetermination of the radio-interference level of high voltage transmission lines — I: Predetermination of the excitation function, *IEEE Trans.*, PAS-91, 284, 1972.
- Moreau, M. R. and Gary, C. H., Predetermination of the radio-interference level of high voltage transmission lines — II: Field calculating method, *IEEE Trans.*, PAS-91, 292, 1972.
- Raether, H., *Electron Avalanche*, Butterworth Co., 1964.
- Trinh, N. G., Partial discharge XX: Partial discharges in air — Part II: Selection of line conductors, *IEEE Electrical Insulation Magazine*, 11, 5, 1995.
- Trinh, N. G., Partial discharge XIX: Discharge in air — Part I: Physical mechanisms, *IEEE Electrical Insulation Magazine*, 11, 23, 1995.
- Trinh, N. G. and Jordan, I. B., Modes of corona discharges in air, *IEEE Trans.*, PAS-87, 1207, 1968.
- Trinh, N. G. and Jordan, I. B., Trichel streamers and their transition into the pulseless glow discharge, *J. Appl. Physics*, 41, 3991, 1970.
- Trinh, N. G. and Maruvada, P. S., A method of predicting the corona performance of conductor bundles based on cage test results, *IEEE Trans.*, PAS-96, 312, 1977.
- Trinh, N. G., Maruvada, P. S., and Poirier, B., A comparative study of the corona performance of conductor bundles for 1200-kV transmission lines, *IEEE Trans.*, PAS-93, 940, 1974.
- Whitehead, J. B., *Systems of Electrical Transmission*, U.S. Patent No. 1,078,711, 1910.

## 4.9 Geomagnetic Disturbances and Impacts Upon Power System Operation

*John G. Kappenman*

Nearly all modern technology systems (power systems, communications, satellites, and navigation to name a few) are more susceptible to geomagnetic disturbances than their counterparts of previous solar cycles. This is certainly the pattern that has been witnessed in the electric power industry.

Geomagnetic disturbances can induce near DC ( $f < 0.01$  Hz) currents (i.e., Geomagnetically Induced Currents, GIC) to flow through the power system entering and exiting the many grounding points on a transmission network. This is generally of most concern at the latitudes of the northern U.S., Canada, and northern Europe, for example, but regions much farther south are affected during intense magnetic storms. GICs are caused when the auroral electrojet (a large multimillion ampere current structure in the conductive portion of the ionosphere at an approximate altitude of 100 km) subjects portions of the earth's nonhomogeneous, conductive surface to time-varying fluctuations in the planet's normally quiescent magnetic field. These field fluctuations induce electric fields in the earth which give rise to potential differences between grounding points. The resulting electric field can extend over large regions and essentially behave as an ideal voltage source applied between remote neutral ground connections of transformers in a power system. This voltage potential difference causes a GIC to flow through the transformers and associated power system lines and neutral ground points. Over 100 amps have been measured in the neutral leads of transformers in such areas, while only a few amps are sufficient to initiate disruption of transformer operation. Solar Cycle 22 (the prior 11-year sunspot cycle 1986–97) has been especially important because of the unprecedented impact that storms have had on electric power systems.

## Power System Reliability Threat

Low-level and very small scale investigations of the impact of geomagnetic storms had been underway in the power industry for a number of years (even dating back to observed impacts from a storm in 1940). However, threats to power system integrity are no longer just academic speculation with the events that unfolded during the Great Geomagnetic Storm of March 13, 1989, when the entire Hydro-Québec system (a system serving more than 6 million customers) was plunged into a blackout, triggered by GIC, causing voltage collapse and equipment malfunction. The impact of this particular storm was simultaneously felt over the entire North American continent with most of Hydro-Québec's neighboring systems in the U.S. coming uncomfortably close to experiencing the same sort of voltage collapse/cascading outage scenario.

Additional, though less severe, storm events in September 1989, March 1991, and October 1991 reinforced, for utilities around the world, that geomagnetic disturbances can hamper reliable operation as voltage regulation is impacted, as undesired relay operations occur on important system equipment, and as new areas of vulnerability are exposed from the unintended consequences of interactions of GIC with various advanced technology apparatus and devices that have been added to the grid. In part, utility system impacts have been greater in recent years because of a more severe and active storm cycle than has been experienced over the prior 30 years. On the other hand, this previous benign era has had the effect of lulling designers into neglecting consideration of these possible influences in their design decisions.

Many portions of the North American power grid have all the elements that contribute to susceptibility to geomagnetic storms: located in northern geomagnetic latitudes, near the auroral electrojet current; located in broad areas of highly resistive igneous rock; and dependent upon remote generation sources linked by long transmission lines to deliver energy to load centers. In fact, the evolving growth of the North American transmission grid over the past few decades has made the grid, along with the geological formations occurring in much of North America, the equivalent of a large efficient antenna that is electromagnetically coupled to the disturbance signals produced by fluctuations of the earth's magnetosphere. GIC, when present in transformers on the system, will produce half-cycle saturation of numerous transformers simultaneously across the network. The large geographic scale coupled with the simultaneous and global impact of these storms produces voltage regulation and harmonic effects in each of these transformers in quantities that add in a cumulative fashion. The result is sufficient to overwhelm the voltage regulation capability and the protection margins of equipment over large regions of the network. Combinations of events such as these can rapidly lead to system-wide problems. For example, the Hydro-Québec outage was the end result of over 15 discrete protective-system operations linked into a chain of events. Further, from the initial event to complete blackout, there was a total elapsed time of a mere one and a half minutes — hardly enough time to even assess what was occurring, let alone provide any meaningful human intervention.

Power systems in areas of igneous rock, typical across the Laurentian shield, for instance, are the most vulnerable to the effects of intense geomagnetic activity because the relatively high resistance of igneous rock encourages more current to flow in alternative conductors such as power transmission lines situated above these geological formations. Research has been done to investigate devices to block GIC flow, but they continue to remain too complex and expensive to blanket such a large network/ground topology.

Operational strategies, and decisions on when to implement them, are presently based upon combinations of storm forecasts and alerts and are often confirmed by locally monitored impacts on power system operations that would be due to a storm (i.e., GIC in a transformer neutral). However, as previously noted, storm events can, at times, progress quickly and some operational changes such as generation redispatch can take up to an hour or more to implement. In situations such as this, it is not always possible to respond quickly enough after a storm is confirmed to prevent serious damage. Forecasts as a means of preparing operational strategies have been problematic in that they have, over prior sunspot cycles, been of low reliability. Since operating postures that would harden power systems to effects of geomagnetic disturbances can be risky, costly, and difficult to effectively maintain for extended durations, and since forecasting technology has been so poor, utilities find themselves caught in the paradox of

(1) either implementing response measures prior to a storm confirmation, or (2) awaiting local confirmation to avoid false alarms and hoping reaction time can be rapid enough.

Also important to electric system operators, though perhaps less obvious, is to know when to deactivate these procedures. The intermittent nature of the effects of geomagnetic storms makes it difficult to tell when the storm activity is over. There may be lulls in activity followed by additional, regionally severe activity. Most guidelines are held for a period of time, usually two to four hours, after the last observed indication of geomagnetic activity. The optimal choice of operating procedures depends on the prediction of the level of GIC in the system which, in turn, requires knowledge of the expected storm severity and local manifestation characteristics. Thus, the ability of system operators to maintain and manage grids under geomagnetically disturbed conditions can be significantly enhanced if the severity and duration of geomagnetic disturbances can be predicted accurately.

### Transformer Impacts due to GIC

The primary concern with geomagnetically induced currents (GIC) is the effect that they have on the operation of a large power transformer. Under normal conditions the large power transformer is a very efficient device for converting one voltage level into another. Decades of design engineering and refinement have increased efficiencies and capabilities of these complex apparatus to the extent that only a few amperes of AC exciting current are necessary to provide the magnetic flux for the voltage transformation in even the largest modern power transformer.

However, in the presence of GIC, the near-direct current essentially biases the magnetic circuit of the transformer with resulting disruptions in performance. The three major effects produced by GIC in transformers are (1) the increased reactive power consumption of the affected transformer, (2) the increased even and odd harmonics generated by the half-cycle saturation, and (3) the possibilities of equipment damaging stray flux heating.

Transformers use steel in their cores to enhance their transformation capability and efficiency, but this core steel introduces nonlinearities into their performance. Common design practice minimizes the effect of the nonlinearity while also minimizing the amount of core steel. Therefore, the transformers are usually designed to operate over a predominantly linear range of the core steel characteristics (as shown in blue in Fig. 4.94a), with only slightly nonlinear conditions occurring at the voltage peaks. This produces a relatively small exciting current (blue in Fig. 4.94b). With GIC present, the normal operating point on the core steel saturation curve is offset and the system voltage variation that is still impressed on the transformer causes operation in an extremely nonlinear portion of the core steel characteristic for half of the AC cycle (red in Fig. 4.94a). Hence the term half-cycle saturation.

Because of the extreme saturation that occurs on half of the AC cycle, the transformer now draws an extremely large asymmetrical exciting current. The red waveform in Fig. 4.94b depicts a typical example from field tests of the exciting current from a three-phase 600 MVA power transformer that has 75 amps of GIC in the neutral (25 A per phase). Spectrum analysis reveals this distorted exciting current to be rich in even, as well as odd harmonics. As is well documented, the presence of even a small amount of GIC (3 to 4 amps per phase or less) will cause half-cycle saturation in a large transformer.

Since the exciting current lags the system voltage by  $90^\circ$ , it creates reactive-power loss in the transformer and the impacted power system. Under normal conditions, this reactive loss is very small. However, the several orders of magnitude increase in exciting current under half-cycle saturation also results in extreme reactive-power losses in the transformer. For example, the three-phase reactive power loss associated with the abnormal exciting current of Fig. 4.94b produces a reactive power loss of over 40 MVars for this transformer alone. The same transformer would draw less than 1 MVar under normal conditions. Figure 4.95 provides a comparison of reactive power loss for two core types of transformers as a function of the amount of GIC flow.

Under a geomagnetic storm condition in which a large number of transformers are experiencing a simultaneous flow of GIC and undergoing half-cycle saturation, the cumulative increase in reactive power demand can be significant enough to impact voltage regulation across the network, and in extreme

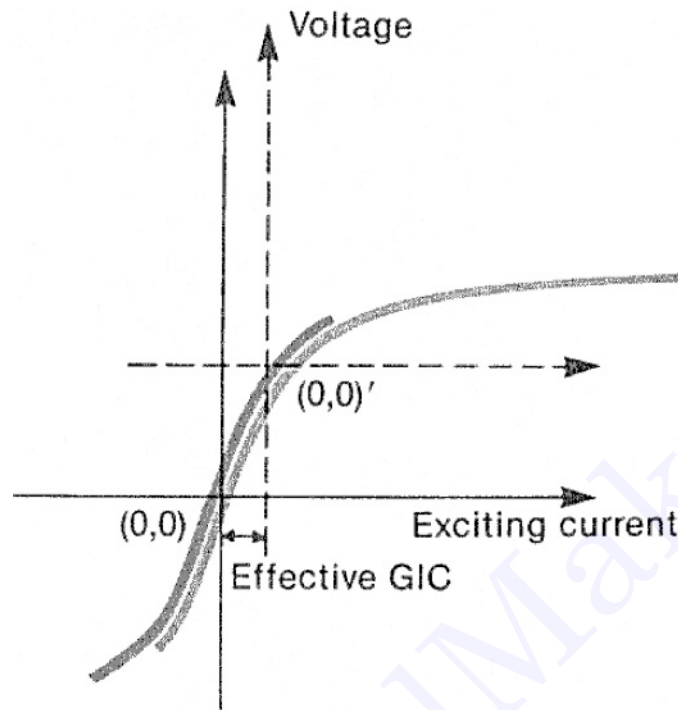


**FIGURE 4.94a** The presence of GIC causes the transformer magnetization characteristics to be biased or offset due to the DC. Therefore on one-half of the AC cycle, the transformer is driven into saturation by the combination of applied voltage and DC bias. Normal excitation operation is shown in the left curve, the biased operation in the right.

situations, lead to network voltage collapse. In the March 13, 1989, superstorm, Manitoba Hydro observed dramatic increases in reactive power output from synchronous condensers at one of their substations. The total reactive requirements at this station alone increased by 420 MVars during the course of the storm event within a few minutes time span. Studies of impacts across a system indicate probable and extreme storm events can cause system-wide reactive demand increases of several thousand MVars. A system GIC flow distribution model taking into account the transformer specific design and GIC flow can provide a means of evaluating the potential for system-wide GIC voltage regulation impacts.

The large and distorted exciting current drawn by the transformer under half-cycle saturation poses a hazard to operation of the network because of the rich source of even and odd harmonic currents this injects into the network and the undesired interactions that these harmonics may cause with relay and protective systems or other power system apparatus. Figure 4.96 is the spectrum analysis of the asymmetrical exciting current from Fig. 4.94b. Even and odd harmonics are present typically in the first ten-orders and the variation of harmonic current production varies somewhat with the level of GIC and the degree of half-cycle saturation. A larger GIC and resulting larger degree of saturation may actually decrease the total harmonic distortion produced by the transformer as more fundamental frequency current is drawn on each half-cycle of saturated operation. An example of this relationship is shown in Fig. 4.97.

In addition to the power system effects of the harmonics and reactive power demands, the transformer itself can be severely stressed by this mode of operation. Measurements have shown that audible noise from the transformer can increase more than fivefold because the magnetostriction of saturated operation increases core steel vibration. Figure 4.98 provides an example of the spectral content of the transformer audible noise variation for various levels of DC excitation. Many anecdotal observations of power system impacts due to geomagnetic disturbances have been as a result of reported transformer audible noise increases.

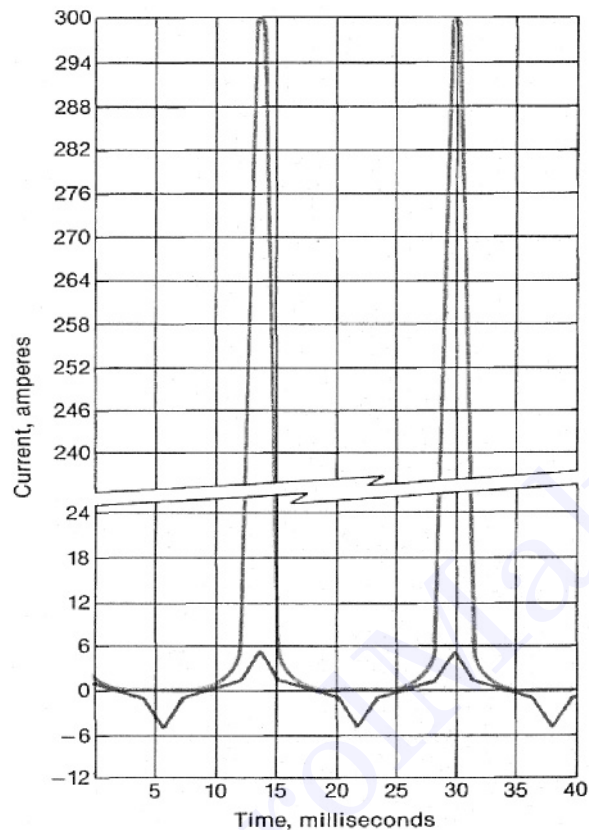


**FIGURE 4.94b** Under normal conditions, the excitation current of this 600 MVA 500/230 kV transformer is less than 1% of transformer rated current. However, with 25 amps/phase of GIC present, the excitation current drawn by the transformer (top curve) is highly distorted by the half-cycle saturation conditions and has a large peak magnitude rich in harmonics.

With the magnetic circuit of the core steel saturated, the magnetic core will no longer contain the flow of flux within the transformer. This stray flux will impinge upon or flow through adjacent paths such as the transformer tank or core clamping structures. The flux in these alternate paths can concentrate to the densities found in the heating elements of a kitchen stove. This abnormal operating regime can persist for extended periods as GIC flows from storm events can last for hours. The hot spots that may then form can severely damage the paper winding insulation, produce gassing and combustion of the transformer oil, or lead to other serious internal failures of the transformer. Such saturation and the unusual flux patterns which result, are not typically considered in the design process and, therefore, a risk of damage or loss of life is introduced. Further a transformer's vulnerability is extremely design dependent, so general conclusions are inappropriate.

One of the more thoroughly investigated incidents of transformer stray flux heating occurred in the Allegheny Power System on a 350 MVA 500/138 kV autotransformer at their Meadow Brook Substation near Winchester, Virginia. The transformer was first removed from service on March 14, 1989, because of high gas levels in the transformer oil which were a by-product of internal heating. The gas-in-oil analysis showed large increases in the amounts of hydrogen, methane, and acetylene, indicating core and tank heating. External inspection of the transformer indicated four areas of blistering or discolored paint due to tank surface heating. In the case of the Meadow Brook transformer, calculations estimate the flux densities were high enough in proximity to the tank to create hot spots approaching 400°C. Reviews made by Allegheny Power indicated that similar heating events (though less severe) occurred in several

### Transformer Reactive Demand

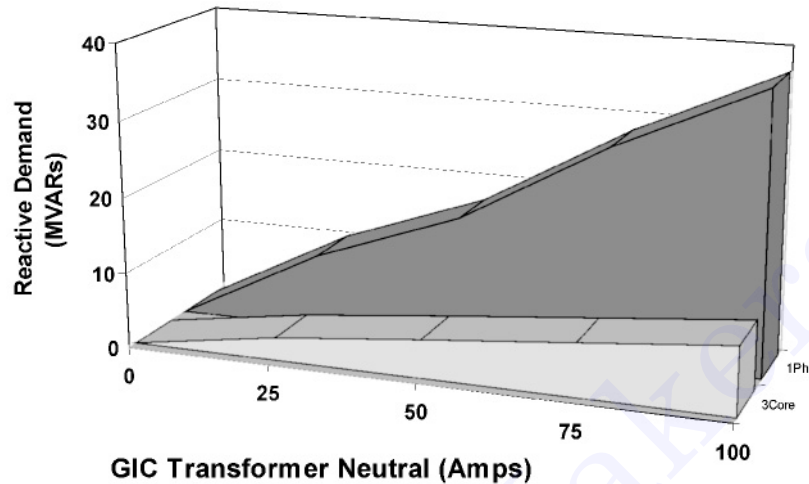


**FIGURE 4.95** The exciting current drawn by half-cycle saturation conditions shown in Fig. 4.94b produces a reactive power loss in the transformer as shown in the top plot. This reactive loss varies with GIC flow as shown. This was measured from field tests of a 3-phase bank of single-phase 500/230 kV transformers. Also shown in the bottom curve is measured reactive demand vs. GIC from a 230/115 kV 3-phase 3-legged core-form transformer. Transformer core design is a significant factor in estimating GIC reactive power impact.

### Transformer Harmonics

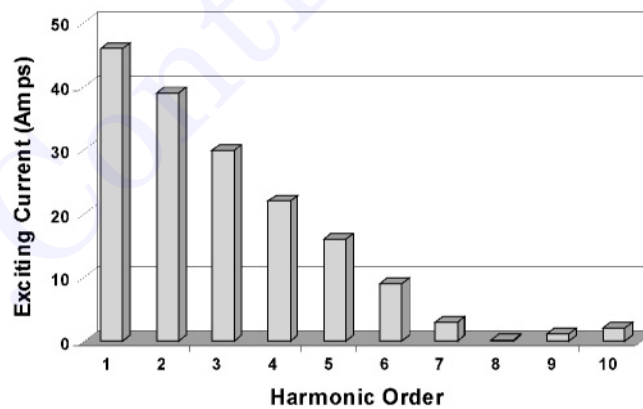


**FIGURE 4.96** The distorted transformer exciting current shown in Fig. 4.94b has even and odd harmonic current distortion. This spectrum analysis was half-cycle saturation conditions resulting from a GIC flow of 25 amps per phase.

other large power transformers in their system due to the March 13 disturbance. Figure 4.99 is a recording that Allegheny Power made on their Meadow Brook transformer during a storm in 1992. This measurement shows an immediate transformer tank hot-spot developing in response to a surge in GIC entering the neutral of the transformer, while virtually no change is evident in the top oil readings. The manufacturer had not predicted or anticipated this mode of operation and therefore could not expect standard over-temperature sensors to be effective deterrents.

Designing a large transformer that would be immune to the near-DC geomagnetically induced current would be technically difficult and prohibitively costly. The ampere-turns of excitation (the product of

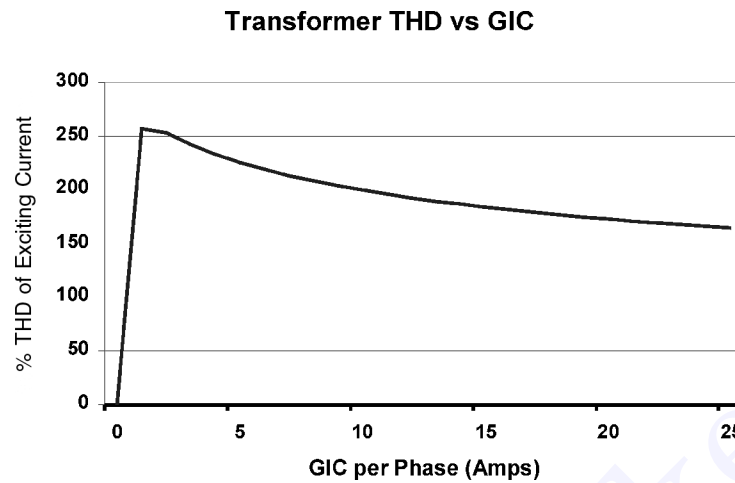


FIGURE 4.97 The total harmonic distortion (THD) of the transformer excitation current is shown above. While the excitation current magnitude increases substantially with increasing GIC flow, the THD percentage decreases as more fundamental frequency excitation current is drawn by the half-cycle saturated transformer.

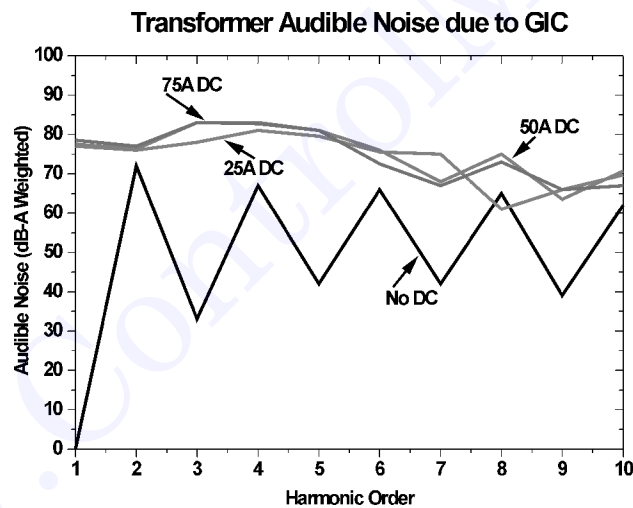
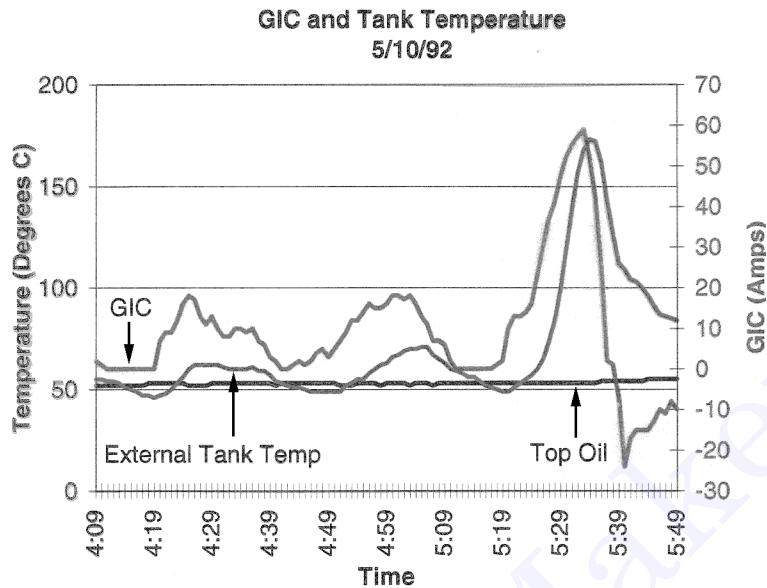


FIGURE 4.98 Half-cycle saturation produces substantial increases in audible noise emissions from a transformer due to core steel magnetostriction. Because the saturation is asymmetrical, the normal 120-Hz hum noise spectrum is replaced by 60 Hz and harmonic noise spectrum.

the normal exciting current and the number of winding turns) generally determine the core steel volume requirements of a transformer. However, designing for unsaturated operation with the high level of GIC present would require a core of excessive size. Blocking the flow of GIC into a transformer is an alternate approach and several design options have been developed for blocking capacitors to install in the transformer neutral. While effective in blocking the flow of GIC for single winding designs, in the case of an autotransformer, the flow of GIC can predominate in the series winding, and as a result, the transformer can still experience severe half-cycle saturation. Series capacitors at the high voltage level can also be employed for GIC blocking but efficacy of GIC mitigation in complex networks requires detailed storm and GIC flow modeling simulations.



**FIGURE 4.99** Transformer hot-spot heating due to stray flux can be a concern in operation of a transformer with GIC present. This transformer experienced stray flux heating that could be monitored with a thermocouple mounted on the tank exterior surface. This storm demonstrated that the GIC and resulting half-cycle saturation produced a rapid heating in the tank hot-spot. Notice also that transformer top-oil temperature did not show any significant change, indicating that the hot-spot was relatively localized.

### Magneto-Telluric Climatology and the Dynamics of a Geomagnetic Superstorm

The sunspot cycle (a measure of variable sunspot observations) is the traditionally defined metric of solar activity. However, impacts at earth due to solar activity are separately defined by the geomagnetic storm cycle. These two cycles are not perfectly in synchronism as shown in Fig. 4.100. The geomagnetic storm cycle tends to have two or three peaks of activity during the course of a typical solar cycle and also presents a broader plateau of higher frequency of activity than implied by the narrower peak of the sunspot cycle. Further geomagnetic activity tends to peak during the declining phase of the sunspot cycle rather than coincident with the sunspot peak. The disconnect between the sunspot cycle and the geomagnetic storm cycle is primarily due to differing solar processes (coronal hole activity) that come into play during the latter half of the solar cycle. These coronal hole processes are not measured by the traditional sunspot count, yet can become the primary driver for geomagnetic storm activity during this stage in the cycle.

Long-term projections of solar cycle activity and expected terrestrial manifestations is more art than science at present owing to the fundamental data and knowledge gaps that exist in understandings of solar processes that drive the solar cycle. As a result, statistical data analysis and trending methods are one of the key inputs in developing projections for upcoming solar cycles, and this is still true for the consensus projections developed for Cycle 23. The consensus opinion holds that Cycle 23 will be a cycle similar in characteristics to Cycle 22, which was in the top quartile of the 22 solar cycles on record (Joselyn et al.). Therefore, this forecast implies an early ascent in activity with the majority of sunspot activity to occur by year 2002. Further, the frequency and severity of geomagnetic storm events is projected to place this solar cycle in the top quartile of severity, even for the lowest projection estimate. Figure 4.101 provides a summary of severe geomagnetic storms over the limited database of measured Ap index (1932 to present). Ap is a measure of the daily range of magnetic field variation at several globally distributed stations. While not directly a measure of GIC production at any specific location, its value stems from

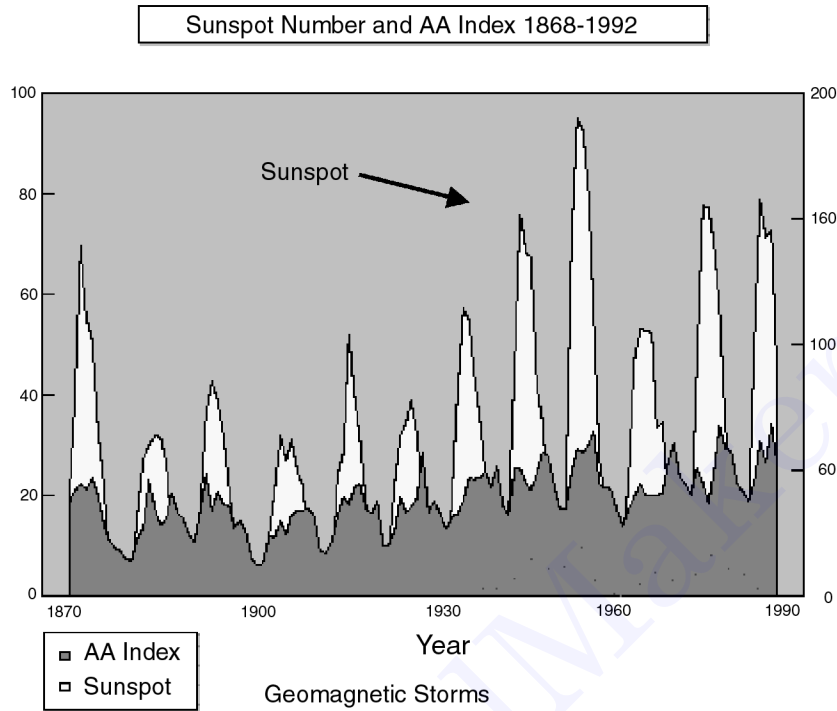


**FIGURE 4.100** The sunspot cycle provides a measure of solar variability. The geomagnetic cycle is the measure of magnetic disturbances at the earth caused by solar activity. The two cycles have different peak and duration characteristics because of solar activity drivers that are not captured by the sunspot count.

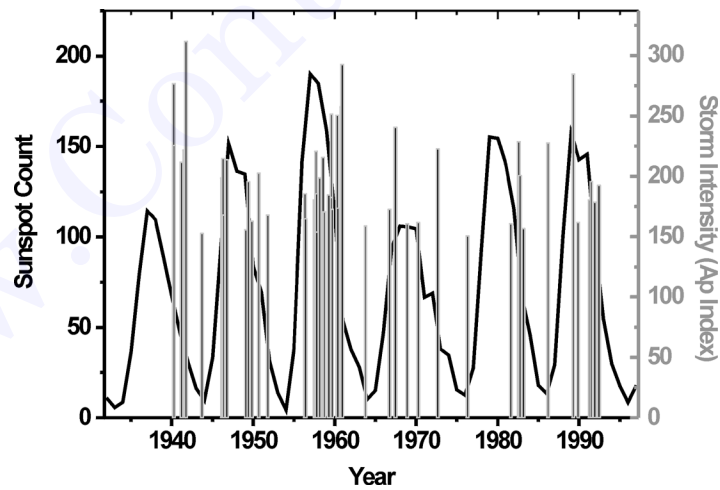


**FIGURE 4.101** The climatology of large geomagnetic storms ( $A_p > 150$ ) is shown over the last 68 years relative to the sunspot cycle. Storms this large have been sufficient to cause large GIC flows with resulting power system impacts. A storm of  $A_p > 150$  occurs approximately 1.06 times per year. Large storms can also occur at any time during the solar cycle and are not confined to the peak sunspot count years.

the fact that it is one of the oldest measures of storm intensity for long-term climatology comparisons. Even this measure is relatively recent, dating back to only 1932, about six solar cycles. Each storm is unique in many aspects, especially in time- and region-specific geomagnetic fluctuations and intensities.

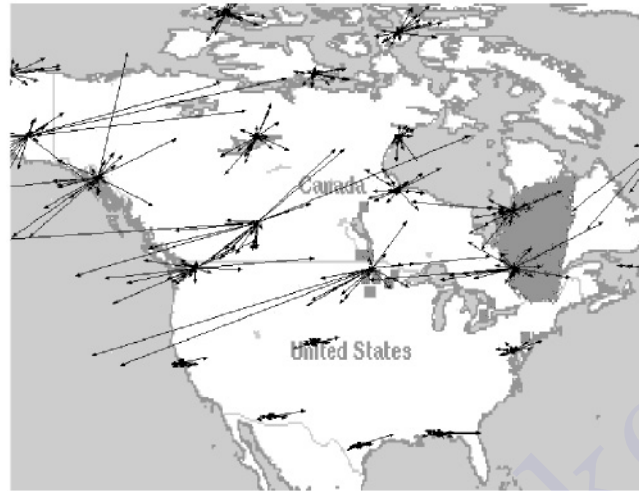


**FIGURE 4.102** Disturbance conditions observed (dBh/dt in nT/min) at North American magnetic observatories on March 13, 1989, between 02:36–03:02 EST and resulting power system impacts reported to NERC. Glen Lea (near Winnipeg) reported the largest dBh/dt of 869 nT/min. The Hydro-Québec system experienced a complete system collapse at approximately 02:45 EST.

Indices, by their nature, provide an averaging of the highly specific impacts over broad windows of time and regions of space and as such tend to blur the details of the spatial dynamics of the electrojet current driver in the ground induction manifestations of a geomagnetic storm.

While the Ap index is imperfect as an absolute measure of GIC impact, it generally takes a storm of Ap intensity of 150 or greater to trigger significant power system events. Given these limitations, a review of Ap index tendencies indicates that a storm of this intensity occurs on a planetary basis at a rate of 1.06 times per year. Further large storms, while more frequent during geomagnetic storm cycle peaks, can occur at any time as they only need one well-aimed eruption from the sun to be created (a solar process that still occurs several times per week even during solar quiet conditions). A good case in point is the 225 Ap storm that shook large parts of the North American power grid in February 1986, the absolute minimum between Sunspot Cycles 21 and 22. The March 13–14, 1989, superstorm was the third largest on record with an Ap of 285. While Cycle 22 produced several noteworthy storm events, the worst cycle of record for large storms was Cycle 19, which produced six storms of Ap 200 or greater versus only two in Cycle 22.

A geomagnetic disturbance produces the large ionospheric current structures that predominate in the nighttime regions of the planet. Spatial and intensity variations in the electrojet interact with the local geomagnetic field and cause intense and impulsive geomagnetic field fluctuations to drive the ground induction process. The electrojet current storm process can be exceedingly large, both in intensity and geographic breadth. In addition, severe and periodic substorms can extend for excessively long durations (several days is typical for large storms). The fluctuations in the million ampere plus electrojet structure produce comparably severe and sudden fluctuations in the ground-level magnetic field in proximity to the electrojet. The coupling of these magnetic field perturbations with the earth and overlaying transmission grid will trigger flows of geomagnetically induced currents (GIC) that can cause transformer half-cycle saturation and associated power system impacts. [Figures 4.102](#) and [4.103](#) summarize the dynamic and widespread impact that the superstorm of March 13, 1989, presented across the North American continent. The time period from 02:30–07:00 EST produced the largest rate of change of ground horizontal magnetic field (dBh/dt variations measured in nano-Tesla per minute) in a region centered on the U.S.-Canadian border. Later substorm events as noted in the time period from 17:00–21:00 EST produced severe dBh/dt events further south, with the largest events occurring over a region from the Canadian border down to the Fredericksburg, VA, and Boulder, CO, observatories. Even

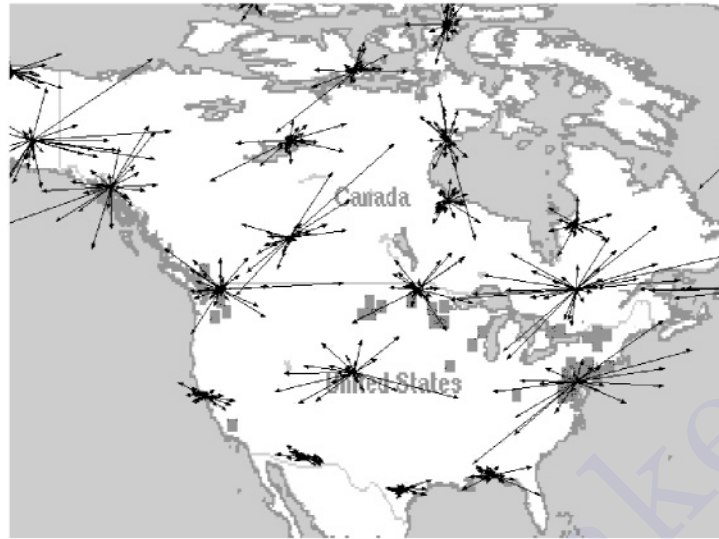


**FIGURE 4.103** Disturbance conditions observed (dBh/dt in nT/min) at North American magnetic observatories on March 13, 1989, between 17:00–17:30 EST and resulting power system impacts reported to NERC. The extent of the storm electrojet structure extended further equatorward, resulting in system impacts through many midlatitude locations.

the Bay St. Louis observatory near the Gulf of Mexico experienced several dBh/dt fluctuations in excess of 300nT/min during this series of substorms. From the observation of large dBh/dt at various observatories around the world during this storm, a plot of geomagnetic field disturbance extrema can be projected on a world map showing equatorward extensions of large dBh/dt events. The projection provides a correction for the asymmetry between the geographic and geomagnetic poles and translates to the appropriate geographic coordinates that these impulsive shocks would extend worldwide.

Figures 4.104 and 4.105 characterize the dBh/dt variations and onsets that are the important drivers for ground-induction, these figures also denote significant region-specific power system impacts that occurred associated with the storm. As shown in Fig. 4.103, the onset of severe magnetic field fluctuations

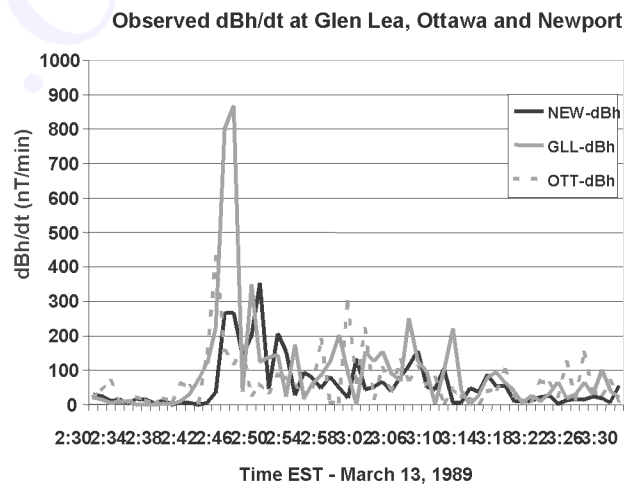


**FIGURE 4.104** Observed dBh/dt (nT/min) at magnetic observatories near the U.S.-Canadian border during the time of the Hydro-Québec blackout and other noteworthy power system impacts.

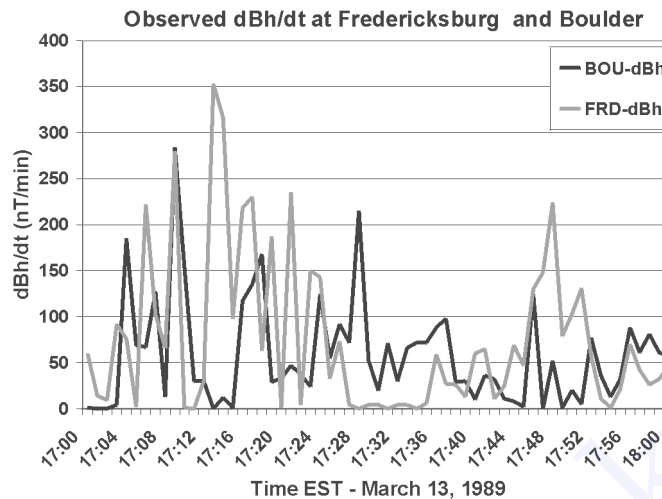


**FIGURE 4.105** Observed dBh/dt (nT/min) at magnetic observatories at U.S. midlatitude sites during a substorm from 17:00–18:00 EST. A large number of transmission network events were reported coincident with these severe disturbances.

can be rapid and essentially allow no lead time for meaningful response measures. Therefore, reacting on the basis of locally observed confirmation of storm activity (such as a measured GIC) would not provide fail-safe lead time especially in the case of the large and important storm events. While NOAA and other governmental agency forecast products would continue to emphasize environmental assessment, impacted systems need additional translation of these broad environmental conditions into potential impacts on their respective systems. Advanced modeling techniques satisfy these industry-specific translation needs.

### Satellite Monitoring and Forecast Models Advance Forecast Capabilities

In January 1998, a NASA satellite (Advanced Composition Explorer or ACE satellite) began providing continuous and real-time monitoring of the solar-wind conditions that are the primary drivers for a geomagnetic storm. The data is fundamental to enabling the formulation of highly accurate forecast techniques and the subsequent issuance of alerts and warnings of impending major geomagnetic disturbances. Because it takes a disturbance in the solar wind about an hour to travel from where ACE is, near the L1 point (about 1 million miles upstream in the solar wind) to earth, telemetry from ACE will allow alerts of imminent, severe geomagnetic storms to be issued nominally an hour in advance of their onset. Data from the ACE satellite and its array of instruments will provide virtually fail-safe certainty in the forecast of major disturbances on a planetary scale.

Unlike the terrestrial weather conditions that are monitored routinely at thousands of locations worldwide, the conditions in space are much more difficult to monitor; therefore, only a handful of space-based and ground-based monitoring stations are available. As a result, space weather forecasters are required to specify and to predict conditions in space and earth’s magnetosphere using a minimum of guidance from actual measurements. The extreme under-sampling of the diverse, coupled regions of space demands that numerical models be utilized to provide continuous quantitative assessment and prediction of the geospace environment. As discussed in the last section, a geomagnetic disturbance can have a rapid and dynamic onset, which, if monitored locally at the earth, would not be able to provide impacted systems meaningful “lead time” for severe storm activity. As evidenced by the concern about system-collapse-type scenarios in operation of transmission networks, remedial measures applied in response to locally detected storm events cannot assure any degree of success in severe storm scenarios.

Therefore, forecast or predictive modeling of space weather is needed if an impacted system requires an advance warning of storm conditions in order to take preventive or mitigative actions. In order to perform the evaluation for the power industry, a number of model development and storm database review procedures were undertaken in order to extend forecasts from planetary-level quality to region-specific projections of severe geomagnetic field disturbances. Solar wind velocity, density, and direction and magnitude of the interplanetary magnetic field provide basic inputs to forecast models which in turn provide an equivalent “lead-time” of a storm event for the processes modeled. These efforts are developing capabilities to predict not only on a global scale, but also more importantly, for concerned transmission grid operators, an ability to provide a projection of region and time-specific meso-scale processes of concern. Further, these can be provided with the expectation that major events can be forecast with a low false alarm rate (Maynard, 1995; Kappenman, 1998).

NOAA and other governmental agencies provide “Environmental Assessments” of forecast storm conditions, whereas power-industry users of forecasts who are responsible for important operational functions during storm events need to have a “System Impact Assessment” of the storm potential. The primary focus of system impact analysis is the desire to quantify the region, system-specific severity, and impact of a storm. NOAA’s forecasts, for example, primarily provide forecast products in index-style severity classification. The most familiar NOAA index is the “K Index,” a logarithmic scale from 0 to 9 that classifies storm severity in a manner similar to the Richter scale for earthquakes. Index approaches are inherently difficult to apply for system impact analysis on power systems, in that the ground-induction process requires detailed knowledge of the electrojet current location and temporal variations. In contrast, indices are derived from averaging that highly detailed information over broad regions and time windows. However, as shown in Figs. 4.102–4.105, sudden and dramatic dB/dt variations and onsets are the important drivers for ground-induction. Therefore, the index approach only “blurs” the induction process details. While NOAA and other governmental agency forecast products will continue to emphasize environmental assessment, impacted systems need additional translation of these broad environmental conditions into potential impacts on their respective systems. Advanced modeling techniques satisfy these industry-specific translation needs.

Since preventing the flow of GIC in power systems is usually not a viable threat mitigation strategy, a management plan to prepare the system for the stress imposed by a resulting geomagnetic is the most prudent course of action. Decisions on when to implement operation measures have been problematic in the past because of the inherent low quality of forecasts that have been provided. Further storm onsets can develop suddenly and as a result, some operation changes cannot be implemented in time to address the paramount priority of system reliability. Forecasts prior to the deployment of the ACE satellite have been very unreliable (less than a 40% accuracy rate with numerous false alarms as well as missed disturbances). The recent deployment of the ACE satellite will provide highly accurate and reliable advance warnings of solar wind conditions that will trigger geomagnetic storm conditions.

Extremely large magnitude magnetic field disturbances can be produced during the course of a severe geomagnetic disturbance. For accurate impact assessment to operational power system forecast users, the forecast needs to provide for the following forecast aspects: (1) a lead time of onset of the most severe portion of the storm event, (2) an intensity prediction of ground level B field deviation and resulting E field, and (3) an expected duration of severe storm conditions. Further, to provide client-specific impact assessment, the definition of the positional and intensity definition of the electrojet current structure has to be specified to provide for a first-order assessment of the ground-induction coupling potential to nearby transmission grids.

The forecasting of the electrojet current structure is a highly refined specification of the environment resulting during the course of a storm event. This refined electrojet environment data can then be used in an electromagnetic coupling model to ground-based systems to provide a first-order assessment of the storm event impact on the modeled ground-based system. System impact forecast assessment capability would provide specific power systems with the ability (through detailed modeling of their respective systems) to evaluate the threat potential of various levels of geomagnetic storm activity and the potential impact that the threat poses to reliable operation. In this example, the magnetosphere and ionosphere

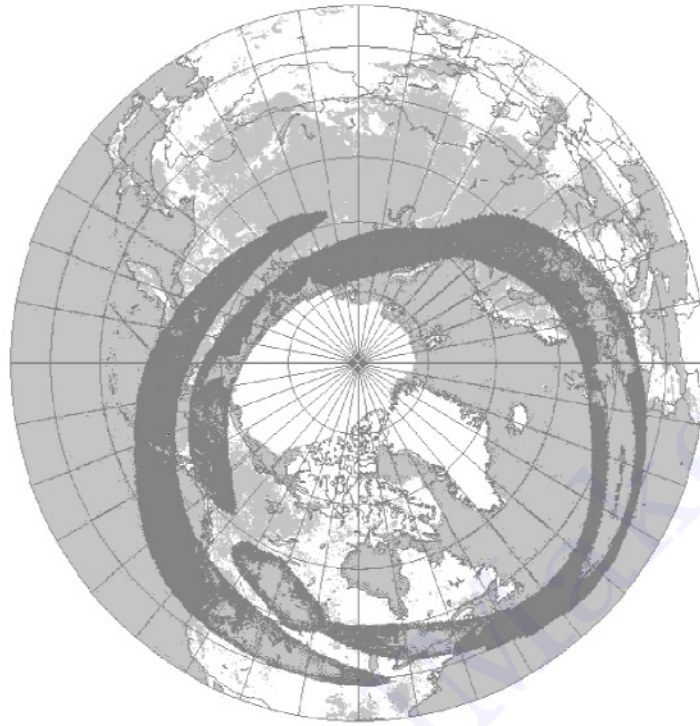


**FIGURE 4.106** Ionospheric model output projecting 45 minutes in advance the electrojet current location and intensity for the May 4, 1998, storm at time UT 04:00. This model output is derived from a magnetospheric/ionospheric model that forecasts these storm patterns typically 45 minutes in advance. The model uses real-time solar wind data from the NASA ACE satellite and updates the model calculation in one-minute time steps.

modeling advances to derive the forecast electrojet current is then coupled with ground-induction modeling to the power system of interest to provide highly reliable and accurate calculations of GIC flows in the networks and resulting voltage regulation impacts with lead times of 45 min or more in advance. Figures 4.106 through 4.109 demonstrate the implementation of the “End-to-End” modeling of a storm-onset-to-power-system-impact forecast process.

This progression from solar wind inputs to forecast GIC flow and power system impact would allow power industry users to have specific impact ranges, magnitudes, and locations of the storm event. Then this forecast expected onset and duration could be incorporated into operational evaluation and state-estimation models. This will allow more precise implementation of power network storm operational measures (for example, transfer constraints and curtailments) when absolutely needed for network security, but will also prevent unnecessarily long periods of operational postures that are restrictive of the energy market functions (Kappenman et al., 1997; Albertson and Van Baelen, 1970).

## References

- Albertson, V.D. and Van Baelen, J.A., Electric and magnetic fields at the earth’s surface due to auroral currents, *IEEE Trans. Power Apparatus Syst.*, PAS-89, 578-594, 1970.
- Barnes, P.R. and Van Dyke, J.W., Potential economic costs from geomagnetic storms, *IEEE Special Publication*, 90th 0357-4-PWR, Geomagnetic Storm Cycle 22: Power System Problems on the Horizon, July 1990.
- Boteler, D.H. and Jansen Van Beek, G., Mapping the March 13, 1989, magnetic disturbance and its consequences across North America, *Solar Terrestrial Predictions IV, Proceedings of a Workshop*, Ottawa, Canada, May 18-22, 1992, Volume 3, pages 57-70.

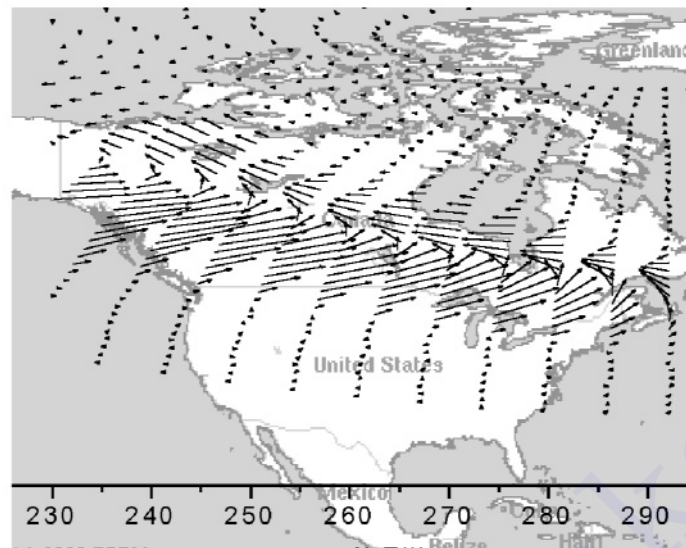


**FIGURE 4.107** A regional view of the electrojet forecast example for May 4, 1998, at 05:00 UT. The electrojet current intensity and location as shown as vector equivalents that are used to electromagnetically couple to client-specific ground-based systems. This provides the first step in the calculation of estimated GIC and power system impact potential due to the geomagnetic storm.

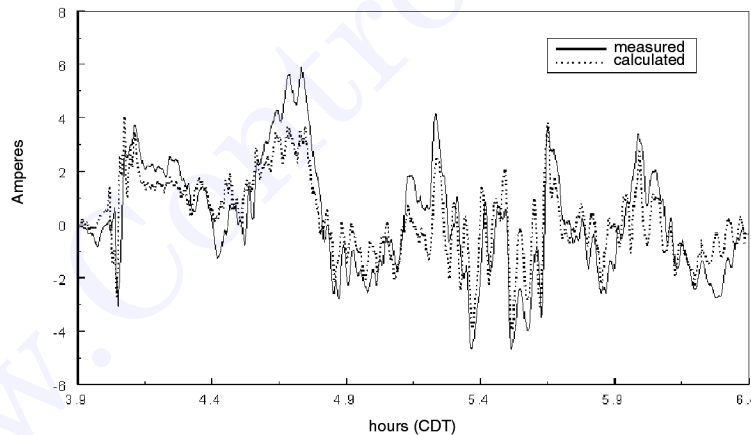


**FIGURE 4.108** Validation of the ground-induction modeling accuracy has shown the ability to replicate GIC flow through transmission networks for storm events with reasonable accuracy over extended time history.

IEEE, The effects of GIC on protective relaying, IEEE Working Group K-11 Report, *IEEE Trans. Power Delivery*, 11(2), 725-739, 1996.

Joselyn J.A. et al., Panel achieves consensus prediction on Solar Cycle 23, *EOS, Trans. Am. Geophys. Union*, 78, 205, 211-212.

Kappenman, J.G., Geomagnetic storm forecasting mitigates power system impacts, *IEEE Power Eng. Rev.*, 4-7, November 1998.

Kappenman J.G. and Albertson, V.D., Bracing for the geomagnetic storms, *IEEE Spectrum Magazine*, March 1990.

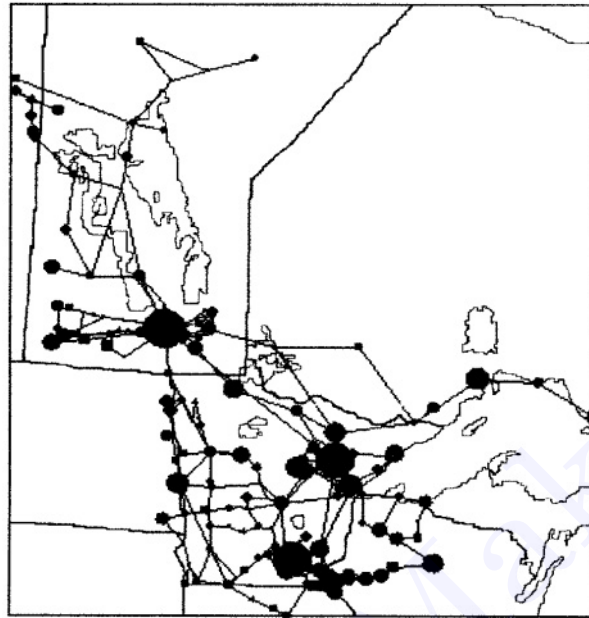


**FIGURE 4.109** With the forecast of the electrojet location and intensity as described in Figs. 4.106 and 4.107, a model of the induction process can be used to calculate the flow of GIC in the power system of interest. With GIC flow calculated in network transformers, projections can be made on the number of transformers that will be driven into half-cycle saturation and the system reactive power losses (MVARs) that will occur.

Kappenman, J.G., Zanetti, L.J., and Radasky, W.A., Space weather from the users perspective: Geomagnetic storm forecasts and the power industry, *EOS, Trans. Am. Geophys. Union*, 78(4), 37, 41, 44-45, 1997.  
 Maynard, N.C., Space weather prediction, *Rev. Geophys.*, Supplement, U.S. National Report to International Union of Geodesy and Geophysics 1991-1994, pg. 547-557, July 1995.

## 4.10 Lightning Protection

*William A. Chisholm*

The study of lightning predates electric power systems by many centuries. Observations of thunder have been maintained in some areas for more than a millenium. Benjamin Franklin and others established the electrical nature of lightning and introduced the concepts of shielding and grounding to protect structures. Early power transmission lines used as many as six overhead shield wires, strung above the phase conductors and grounded at the towers for effective lightning protection. Later in the twentieth century, repeated strikes to tall towers, buildings, and power lines, contradicting the adage that “it never strikes twice,” allowed systematic study of stroke current parameters. Improvements in electronics, computers, telecommunications, rocketry, and satellite technologies have all extended our knowledge about lightning, while at the same time exposing us to ever-increasing risks of economic damage from its consequences.

### Ground Flash Density

The first negative, downward, cloud-to-ground lightning stroke is the dominant risk element to power system components. Positive first strokes, negative subsequent strokes, and continuing currents can also cause specific problems. A traditional indicator of cloud-to-ground lightning activity is given by thunder observations, collected to World Meteorological Organization standards and converted to Ground Flash Density (Anderson et al., 1984; MacGorman et al., 1984):

$$\text{GFD} = 0.04 \text{ TD}^{1.25} \quad (4.154)$$

$$\text{GFD} = 0.054 \text{ TH}^{1.1} \quad (4.155)$$

where

TD = number of days with thunder per year

TH = number of hours with thunder per year

GFD = number of first cloud-to-ground strokes per square kilometer per year

Long-term thunder data suggest that GFD has a relative standard deviation of 30%.

Electromagnetic signals from lightning are unique and have a high signal-to-noise ratio at large distances. Many single-station lightning flash counters have been developed and calibrated, each with good discrimination between cloud-flash and ground-flash activity using simple electronic circuits (Heydt, 1982). It has also been feasible for more than twenty years (Krider et al., 1976) to observe these signals with two or more stations and to triangulate lightning stroke locations on a continent-wide basis. Lightning location networks (Global Atmospheric, Inc., Website, 2000) have improved continuously to the point where multiple ground strikes from a single flash can be resolved with high spatial and temporal accuracy and high probability of detection. A GFD value from these data should be based on approximately 400 counts in each cell to reduce relative standard deviation of the observation process below 5%. In areas with moderate flash density, a minimum cell size of  $20 \times 20$  km is appropriate.

In areas where there are presently no commercial lightning location networks, Optical Transient Detector (OTD) observations from low-earth orbit offer some merit. This class of instrument, first operated systematically in 1995 (GHCC Website, 2000), provides an unbiased quantitative sample of lightning activity over most of the globe. The OTD responds to both cloud and ground flashes, and has some blind areas at the poles and in the south Atlantic near Brazil. However, comparisons of orographic lightning features, such as an elevated flash density to the east of the Rocky Mountains in North America, confirm and extend important trends seen in limited ground-based network observations. The OTD technology is also improving as new satellites build on the successful experiences.

### Stroke Incidence to Power Lines

The lightning leader, a thin column of electrically charged plasma, develops from cloud down to the ground in a series of step breakdowns (Uman, 1987). Near the ground, electric fields are high enough to satisfy the conditions for continuous positive leader inception upward from tall objects or conductors. Analysis of a single overhead conductor with this approach (Rizk, 1990) leads to:

$$N_s = 3.8 \text{ GFD } h^{0.45} \quad (4.156)$$

where

$N_s$  = the number of strikes to the conductor per 100 km of line length per year

$h$  = the average height of the conductor above ground, in meters

In areas of moderate to high ground flash density, one or more overhead shield wires are usually installed above the phase conductors. This shielding usually has a success rate of greater than 95%, but adds nearly 10% to the cost of line construction and also wastes energy from induced currents. The leader inception model (Rizk, 1990) has also been used to analyze shielding failures.

## Stroke Current Parameters

Once the downward leader contacts a power system component through an upward-connecting leader, the stored charge will be impressed through a high channel impedance of 600 to 2000  $\Omega$ . With this high source impedance, an impulse current source model is suitable.

Berger made the most reliable direct measurements of negative downward cloud-to-ground lightning parameters on an instrumented tower from 1947 to 1977 (Berger, 1977). Additional observations have been provided by many researchers and then summarized (Anderson and Eriksson, 1980; CIGRE, 1991). The overall stroke current distribution can be approximated (CIGRE, 1991) as log-normal with a mean of 31 kA and a log standard deviation of 0.48. The waveshape rises with a concave front, giving the maximum steepness near the crest of the wave, then decays with a time to half-value of 50  $\mu$ s or more. The median value of maximum steepness (CIGRE, 1991) is 24 kA/ $\mu$ s, with a log standard deviation of 0.60. Steepness has a positive correlation to the peak amplitude (CIGRE, 1991) that allows simplified modeling using a single equivalent front time (peak current divided by peak rate of rise). The mean equivalent front is 1.4  $\mu$ s for the median 31-kA current, rising to 2.7  $\mu$ s as peak stroke current increases to the 5% level of 100 kA (CIGRE, 1991). An equivalent front time of 2  $\mu$ s is recommended for simplified analysis (IEEE, 1997).

## Calculation of Lightning Overvoltages on Shielded Lines

The voltage rise  $V_R$  of the ground resistance  $R$  at each tower will be proportional to peak stroke current:  $V_R = R I$ . The relation between the tower base geometry and its resistance is:

$$R = \frac{\rho}{2\pi s} \ln \left( \frac{17s^2}{A} \right) + \frac{\rho}{l} \quad (4.157)$$

where

$\rho$  = soil resistivity ( $\Omega$ -m)

$s$  = the three-dimensional distance from the center to its outermost point (m)

$A$  = the surface area (sides + base) of the hole needed to excavate the electrode ( $m^2$ )

$l$  = the length (m) of the wire used to make up the electrode (infinite for solid electrodes)

For large surge currents, local ionization will tend to reduce the second  $\rho/l$  contact resistance term but not the first geometric resistance term in Eq. (4.157).

The voltage rise  $V_L$  associated with conductor and tower series inductance  $L$  and the equivalent front time ( $dt = 2 \mu$ s) is  $V_L = L I/dt$ . The  $V_L$  term will add to, and sometimes dominate,  $V_R$ . Lumped inductance can be approximated from the expression:

$$L = Z \tau = 60 \ln \left( \frac{2h}{r} \right) \times \frac{l}{c} \quad (4.158)$$

where

$L$  = the inductance (H)

$Z$  = the element antenna impedance ( $\Omega$ )

$h$  = the wire height above conducting ground (m)

$r$  = the wire radius (m)

$l$  = the wire length (m)

$c$  = the speed of light ( $3 \times 10^8$  m/s)

In numerical analyses, series and shunt impedance elements can be populated using the same procedure. Tall transmission towers have longer travel times and thus higher inductance, which further exacerbates the increase of stroke incidence with line height. The high electromagnetic fields surrounding any stricken conductor will induce currents and couple voltages in nearby, unstricken conductors through their mutual surge impedances. In the case where lightning strikes a grounded overhead shield wire, this coupling increases common-mode voltage and reduces differential voltage across insulators. Additional shield wires and corona (CIGRE, 1991; IEEE, 1997) can improve this desirable surge-impedance coupling to mitigate half of the total tower potential rise ( $V_R + V_L$ ).

The strong electromagnetic fields from vertical lightning strokes can induce large overvoltages in nearby overhead lines without striking them directly. This is a particular concern only for MV and LV systems.

### Insulation Strength

Power system insulation is designed to withstand all anticipated power system overvoltages. Unfortunately, even the weakest direct stroke from a shielding failure to a phase conductor will cause a lightning flashover. Once an arc appears across an insulator, the power system fault current keeps this arc alive until voltage is removed by protective relay action. Effective overhead shielding is essential on transmission lines in areas with moderate to high ground flash density.

When the overhead shield wire is struck, the potential difference on insulators is the sum of the resistive and inductive voltage rises on the tower, minus the coupled voltage on the phase conductors. The potential difference can lead to a “backflashover” from the tower to the phase conductor. Backflashover is more frequent when the stroke current is large ( $5\% > 100 \text{ kA}$ ), when insulation strength is low ( $< 1 \text{ m}$  or  $600 \text{ kV}$  Basic Impulse Level) and/or when footing resistance is high ( $> 30 \Omega$ ). Simplified models (CIGRE, 1991; IEEE, 1997) are available to carry out the overvoltage calculations and coordinate the results with insulator strength, giving lightning outage rates in units of interruptions per 100 km per year.

### Mitigation Methods

Lightning mitigation methods need to be appropriate for the expected long-term ground flash density and power system reliability requirements. Table 4.27 summarizes typical practices at five different levels of lightning activity to achieve a reliability of one outage per 100 km of line per year on an HV line.

**TABLE 4.27** Lightning Mitigation Methods

Ground Flash Density Range	Typical Design Approaches
0.1–0.3 ground flashes/km <sup>2</sup> per year	Unshielded, one- or three-pole reclosing
0.3–1 ground flashes/km <sup>2</sup> per year	Single overhead shield wire
1–3 ground flashes/km <sup>2</sup> per year	Two overhead shield wires
3–10 ground flashes/km <sup>2</sup> per year	Two overhead shield wires with good grounding or line surge arresters
10–30 ground flashes/km <sup>2</sup> per year	Three or more overhead and underbuilt shield wires with good grounding; line surge arresters; underground transmission cables

*Note:* Designs to achieve reliability of one outage per 100 km of line per year on an HV line.

### Conclusion

Direct lightning strokes to any overhead transmission line are likely to cause impulse flashover of supporting insulation, leading to a circuit interruption. The use of overhead shield wires, located above the phase conductors and grounded adequately at each tower, can reduce the risk of flashover by 95–99.5%, depending on system voltage.

## References

- Anderson, R. B. and Eriksson, A. J., Lightning parameters for engineering applications, *Electra* No. 69, 65-102, 1980.
- Anderson, R. B., Eriksson, A. J., Kroninger, H., Meal, D. V., Lightning and thunderstorm parameters, IEEE Conference Publication 236, *Lightning and Power Systems*, London, June 1984.
- Berger, K., The earth flash, in *Lightning*, Golde, R., Ed., Academic Press, London, 119-190, 1977.
- CIGRE Working Group 01 (Lightning) of Study Committee 33, Guide to Procedures for Estimating the Lightning Performance of Transmission Lines, *CIGRE Brochure 63*, Paris, October 1991.
- Global Atmospheric, Inc.*, Global Atmospheric, Inc., April 10, 2000, (<http://www.glatmos.com>).
- Heydt, G., Instrumentation, in *Handbook of Atmospheric*, Volume II, Volland, H., Ed., CRC Press, Boca Raton, FL, 203-256, 1982.
- IEEE Guide for Improving the Lightning Performance of Transmission Lines*, IEEE Standard 1243-1997, December 1997.
- Krider, E.P., Nogge, R. C, and Uman, M. A., A gated, wideband direction finder for lightning return strokes, *J. Appl. Meteor.*, 15, 301, 1976.
- Lightning and Atmospheric Electricity Research at the GHCC*, Global Hydrology and Climate Center (GHCC), April 10, 2000, (<http://thunder.msfc.nasa.gov/>).
- MacGorman, D. R., Maier, M. W., Rust, W. D., Lightning Strike Density for the Contiguous United States from Thunderstorm Duration Records. Report to U.S. Nuclear Regulatory Commission, NUREG/CR-3759, 1984.
- Rizk, F. A. M., Modeling of transmission line exposure to direct lightning strokes, *IEEE Trans PWRD*, 5(4), 1983, 1990.
- Uman, M. A., *The Lightning Discharge*, Academic Press, New York, 1987.

## 4.11 Reactive Power Compensation

Rao S. Thallam

### The Need for Reactive Power Compensation

Except in a very few special situations, electrical energy is generated, transmitted, distributed, and utilized as alternating current (AC). However, alternating current has several distinct disadvantages. One of these is the necessity of reactive power that needs to be supplied along with active power. Reactive power can be leading or lagging. While it is the active power that contributes to the energy consumed, or transmitted, reactive power does not contribute to the energy. Reactive power is an inherent part of the "total power." Reactive power is either generated or consumed in almost every component of the system, generation, transmission, and distribution and eventually by the loads. The impedance of a branch of a circuit in an AC system consists of two components, resistance and reactance. Reactance can be either inductive or capacitive, which contribute to reactive power in the circuit. Most of the loads are inductive, and must be supplied with lagging reactive power. It is economical to supply this reactive power closer to the load in the distribution system.

In this section, reactive power compensation, mainly in transmission systems installed at substations, is discussed. Reactive power compensation in power systems can be either shunt or series. Both will be discussed.

### Shunt Reactive Power Compensation

Since most loads are inductive and consume lagging reactive power, the compensation required is usually supplied by leading reactive power. Shunt compensation of reactive power can be employed either at load level, substation level, or at transmission level. It can be capacitive (leading) or inductive (lagging) reactive power, although in most cases as explained before, compensation is capacitive. The most common form of leading reactive power compensation is by connecting shunt capacitors to the line.

## Shunt Capacitors

Shunt capacitors are employed at substation level for the following reasons:

1. Voltage regulation: The main reason that shunt capacitors are installed at substations is to control the voltage within required levels. Load varies over the day, with very low load from midnight to early morning and peak values occurring in the evening between 4 PM and 7 PM. Shape of the load curve also varies from weekday to weekend, with weekend load typically low. As the load varies, voltage at the substation bus and at the load bus varies. Since the load power factor is always lagging, a shunt connected capacitor bank at the substation can raise voltage when the load is high. The shunt capacitor banks can be permanently connected to the bus (fixed capacitor bank) or can be switched as needed. Switching can be based on time, if load variation is predictable, or can be based on voltage, power factor, or line current.
2. Reducing power losses: Compensating the load lagging power factor with the bus connected shunt capacitor bank improves the power factor and reduces current flow through the transmission lines, transformers, generators, etc. This will reduce power losses ( $I^2R$  losses) in this equipment.
3. Increased utilization of equipment: Shunt compensation with capacitor banks reduces kVA loading of lines, transformers, and generators, which means with compensation they can be used for delivering more power without overloading the equipment.

Reactive power compensation in a power system is of two types — shunt and series. Shunt compensation can be installed near the load, in a distribution substation, along the distribution feeder, or in a transmission substation. Each application has different purposes. Shunt reactive compensation can be inductive or capacitive. At load level, at the distribution substation, and along the distribution feeder, compensation is usually capacitive. In a transmission substation, both inductive and capacitive reactive compensation are installed.

## Application of Shunt Capacitor Banks in Distribution Systems — A Utility Perspective

The Salt River Project (SRP) is a public power utility serving more than 720,000 (April 2000) customers in central Arizona. Thousands of capacitor banks are installed in the entire distribution system. The primary usage for capacitor banks in the distribution system is to maintain a certain power factor at peak loading conditions. The target power factor is .98 leading at system peak. This figure was set as an attempt to have a unity power factor on the 69-kV side of the substation transformer. The leading power factor compensates for the industrial substations that have no capacitors. The unity power factor maintains a balance with ties to other utilities.

The main purpose of the capacitors is not for voltage support, as the case may be at utilities with long distribution feeders. Most of the feeders in the SRP service area do not have long runs (substations are about two miles apart) and load tap changers on the substation transformers are used for voltage regulation.

The SRP system is a summer peaking system. After each summer peak, a capacitor study is performed to determine the capacitor requirements for the next summer. The input to the computer program for evaluating capacitor additions consists of three major components:

- Megawatts and megavars for each substation transformer at peak.
- A listing of the capacitor banks with size and operating status at time of peak.
- The next summer's projected loads.

By looking at the present peak MW and Mvars and comparing the results to the projected MW loads, Mvar deficiencies can be determined. The output of the program is reviewed and a listing of potential needs is developed. The system operations personnel also review the study results and their input is included in making final decisions about capacitor bank additions.

Once the list of additional reactive power requirements is finalized, determinations are made about the placement of each bank. The capacitor requirement is developed on a per-transformer basis. The

**TABLE 4.28** Number and Size of Capacitor Banks in the SRP System

Kvar	Number of Banks	
	Line	Station
150	1	
300	140	
450	4	
600	758	2
900	519	
1200	835	581
Total	2257	583

**TABLE 4.29** SRP Line Capacitors by Type of Control

Type of Control	Number of Banks
Current	4
Fixed	450
Time	1760
Temperature	38 (used as fixed)
Voltage	5

ratio of the kvar connected to kVA per feeder, the position on the feeder of existing capacitor banks, and any concentration of present or future load are all considered in determining the position of the new capacitor banks. All new capacitor banks are 1200 kvar. The feeder type at the location of the capacitor bank determines if the capacitor will be pole-mounted (overhead) or pad-mounted (underground).

Capacitor banks are also requested when new feeders are being proposed for master plan communities, large housing developments, or heavy commercial developments.

Table 4.28 shows the number and size of capacitor banks in the SRP system in 1998. Table 4.29 shows the number of line capacitors by type of control.

Substation capacitor banks (three or four per transformer) are usually staged to come on and go off at specific load levels.

### Static VAR Control (SVC)

Static VAR compensators, commonly known as SVCs, are shunt connected devices, vary the reactive power output by controlling or switching the reactive impedance components by means of power electronics. This category includes the following equipment:

- Thyristor controlled reactors (TCR) with fixed capacitors (FC)
- Thyristor switched capacitors (TSC)
- Thyristor controlled reactors in combination with mechanically or Thyristor switched capacitors

SVCs are installed to solve a variety of power system problems:

1. Voltage regulation
2. Reduce voltage flicker caused by varying loads like arc furnace, etc.
3. Increase power transfer capacity of transmission systems
4. Increase transient stability limits of a power system
5. Increase damping of power oscillations
6. Reduce temporary overvoltages
7. Damp subsynchronous oscillations

A view of an SVC installation is shown in Figure 4.110.

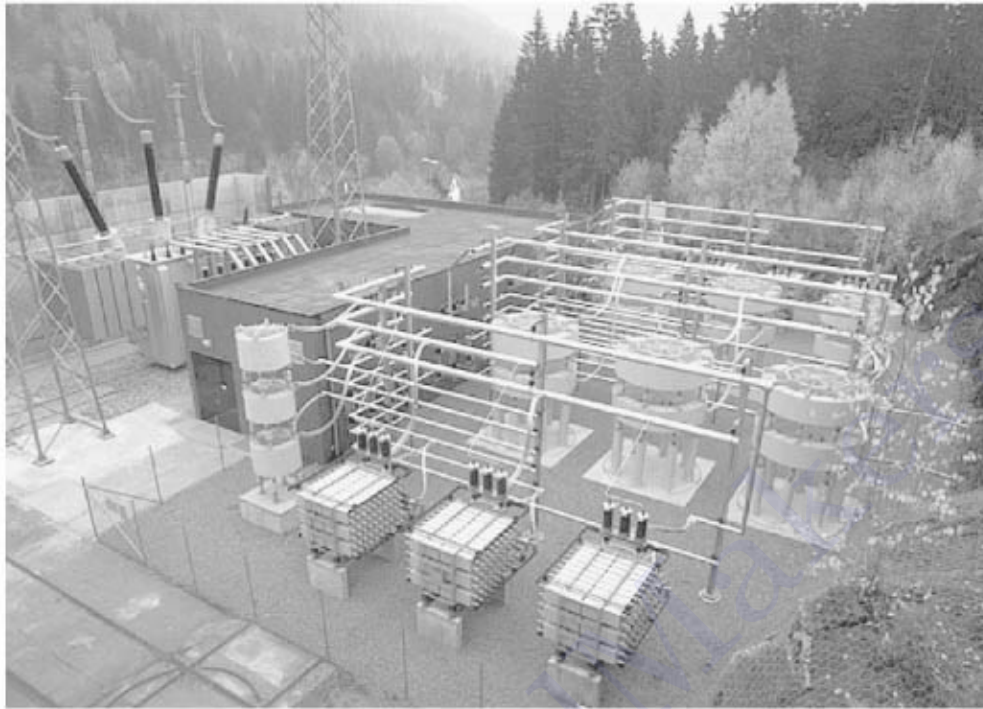


FIGURE 4.110 View of static VAR compensator (SVC) installation. (Photo courtesy of ABB.)

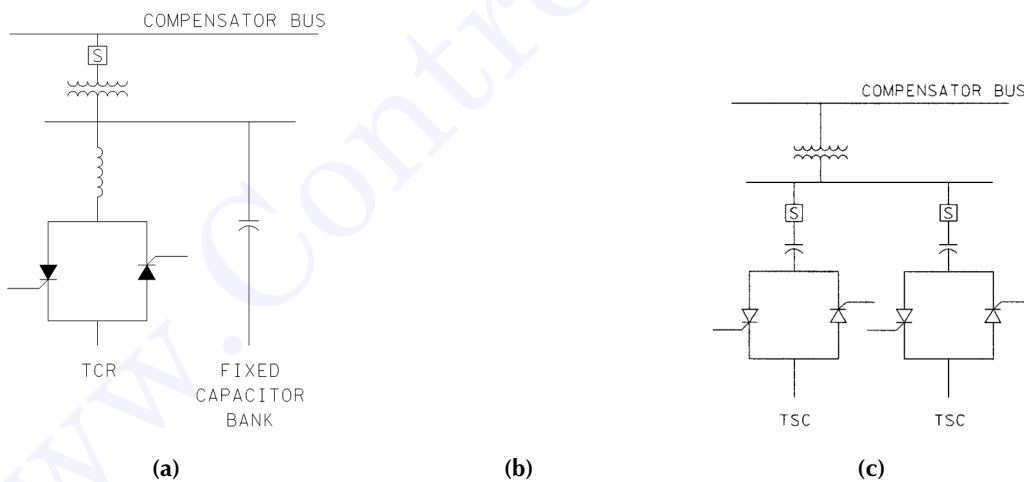


FIGURE 4.111 Three versions of SVC. (a) TCR with fixed capacitor bank; (b) TCR with switched capacitor banks; and (c) thyristor switched capacitor compensator.

### Description of SVC

Figure 4.111 shows three basic versions of SVC. Figure 4.111a shows configuration of TCR with fixed capacitor banks. The main components of a SVC are thyristor valves, reactors, the control system, and the step-down transformer.

### How Does SVC Work?

As the load varies in a distribution system, a variable voltage drop will occur in the system impedance, which is mainly reactive. Assuming the generator voltage remains constant, the voltage at the load bus

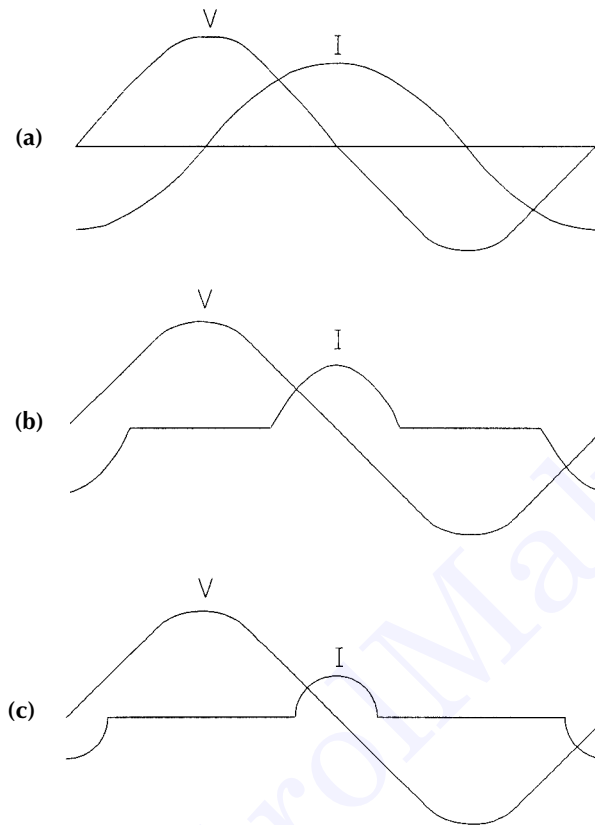


**FIGURE 4.112** TCR voltage (V) and current (I) waveforms for three conduction levels. Thyristor gating angle =  $\alpha$ ; conduction angle =  $\sigma$ . (a)  $\alpha = 90^\circ$  and  $\sigma = 180^\circ$ ; (b)  $\alpha = 120^\circ$  and  $\sigma = 120^\circ$ ; and (c)  $\alpha = 150^\circ$  and  $\sigma = 60^\circ$ .

will vary. The voltage drop is a function of the reactive component of the load current, and system and transformer reactance. When the loads change very rapidly, or fluctuate frequently, it may cause “voltage flicker” at the customers’ loads. Voltage flicker can be annoying and irritating to customers because of the “lamp flicker” it causes. Some loads can also be sensitive to these rapid voltage fluctuations.

An SVC can compensate voltage drop for load variations and maintain constant voltage by controlling the duration of current flow in each cycle through the reactor. Current flow in the reactor can be controlled by controlling the gating of thyristors that control the conduction period of the thyristor in each cycle, from zero conduction (gate signal off) to full-cycle conduction. In Fig. 4.111a, for example, assume the MVA of the fixed capacitor bank is equal to the MVA of the reactor when the reactor branch is conducting for full cycle. Hence, when the reactor branch is conducting full cycle, the net reactive power drawn by the SVC (combination of capacitor bank and thyristor controlled reactor) will be zero. When the load reactive power (which is usually inductive) varies, the SVC reactive power will be varied to match the load reactive power by controlling the duration of the conduction of current in the thyristor controlled reactive power branch. Figure 4.112 shows current waveforms for three conduction levels, 60, 120 and 180°. Figure 4.112a shows waveforms for thyristor gating angle ( $\alpha$ ) of 90°, which gives a conduction angle ( $\sigma$ ) of 180° for each thyristor. This is the case for full-cycle conduction, since the two back-to-back thyristors conduct in each half-cycle. This case is equivalent to shorting the thyristors. Figure 4.112b is the case when the gating signal is delayed for 30° after the voltage peak, and results in a conduction angle of 120°. Figure 4.112c is the case for  $\alpha = 150^\circ$  and  $\sigma = 60^\circ$ .

With a fixed capacitor bank as shown in Figure 4.111a, it is possible to vary the net reactive power of the SVC from 0 to the full capacitive VAR only. This is sufficient for most applications of voltage regulation, as in most cases only capacitive VARs are required to compensate the inductive VARs of the load. If the

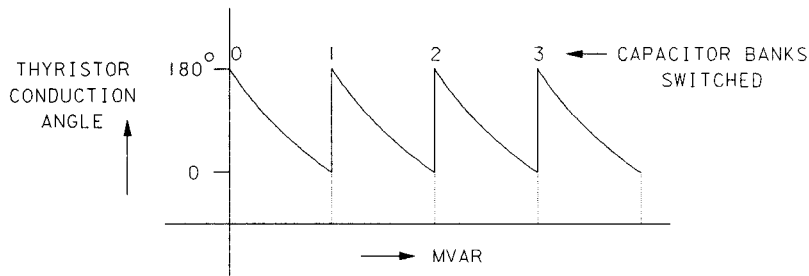


FIGURE 4.113 Reactive power variation of TCR with switched capacitor banks.

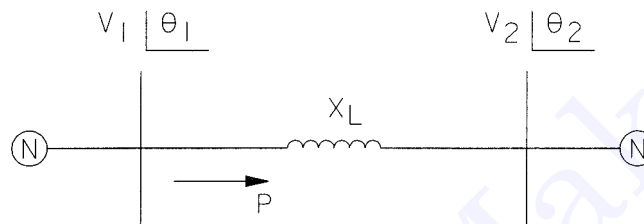


FIGURE 4.114 Power flow through transmission line.

capacitor can be switched on and off, the MVAR can be varied from full inductive to full capacitive, up to the rating of the inductive and capacitive branches. The capacitor bank can be switched by mechanical breakers (see Fig. 4.111b) if time delay (usually five to ten cycles) is not a consideration, or they can be switched fast (less than one cycle) by thyristor switches (see Fig. 4.111c).

Reactive power variation with switched capacitor banks for an SVC is shown in Fig. 4.113.

### Series Compensation

Series compensation is commonly used in high-voltage AC transmission systems. They were first installed in that late 1940s. Series compensation increases power transmission capability, both steady state and transient, of a transmission line. Since there is increasing opposition from the public to construction of EHV transmission lines, series capacitors are attractive for increasing the capabilities of transmission lines. Series capacitors also introduce some additional problems for the power system. These will be discussed later.

Power transmitted through the transmission system (shown in Fig. 4.114) is given by:

$$P_2 = \frac{V_1 \cdot V_2 \cdot \sin \delta}{X_L} \quad (4.159)$$

where

- $P_2$  = Power transmitted through the transmission system
- $V_1$  = Voltage at sending end of the line
- $V_2$  = Voltage at receiving end of transmission line
- $X_L$  = Reactance of the transmission line
- $\delta$  = Phase angle between  $V_1$  and  $V_2$

Equation (4.159) shows that if the total reactance of a transmission system is reduced by installing capacitance in series with the line, the power transmitted through the line can be increased.

With a series capacitor installed in the line, Eq. (4.159) can be written as

$$P_2 = \frac{V_1 \cdot V_2 \cdot \sin \delta}{X_L - X_C} \quad (4.160)$$

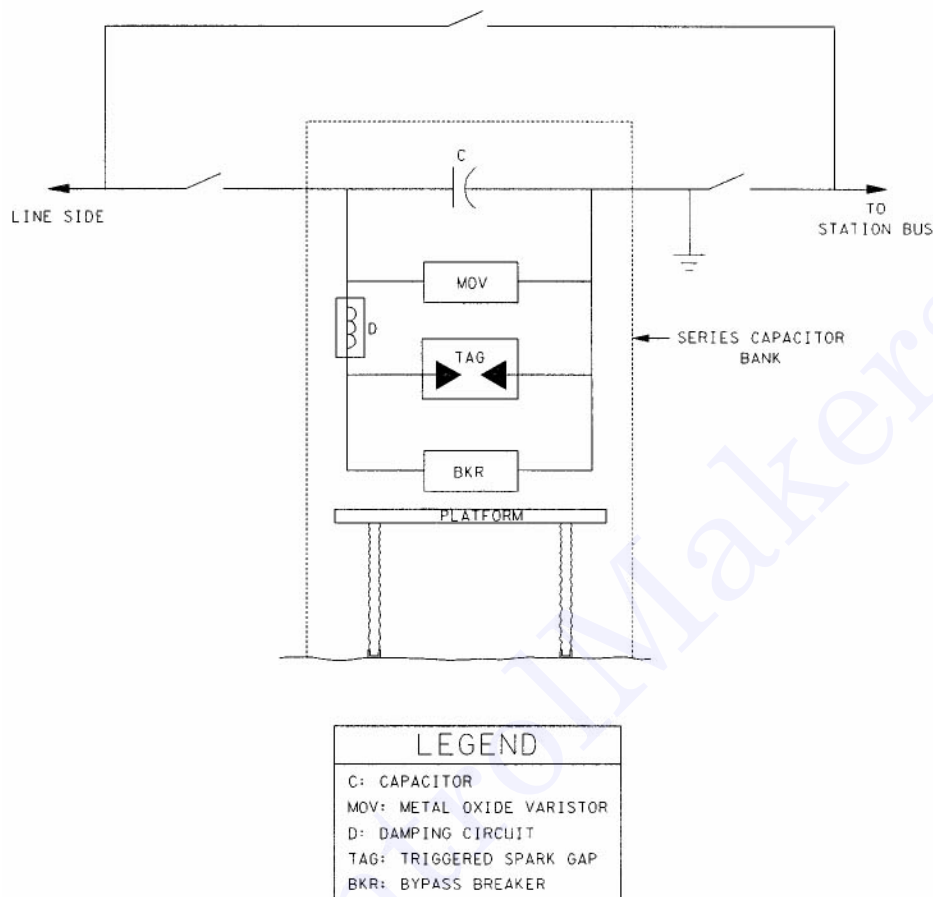


FIGURE 4.115 Schematic one-line diagram of series capacitor bank.

$$= \frac{V_1 \cdot V_2 \cdot \sin \delta}{X_L (1 - K)} \tag{4.161}$$

where  $K = \frac{X_C}{X_L}$  is degree of the compensation, usually expressed in percent. A 70% series compensation means the value of the series capacitor in ohms is 70% of the line reactance.

### Series Capacitor Bank

A series capacitor bank consists of a capacitor bank, overvoltage protection system, and a bypass breaker, all elevated on a platform, which is insulated for the line voltage. See Fig. 4.115. The overvoltage protection is comprised of a zinc oxide varistor and a triggered spark gap, which are connected in parallel to the capacitor bank, and a damping reactor. Prior to the development of the high-energy zinc oxide varistor in the 1970s, a silicon carbide nonlinear resistor was used for overvoltage protection. Silicon carbide resistors require a spark gap in series because the nonlinearity of the resistors is not high enough. The zinc oxide varistor has better nonlinear resistive characteristics, provides better protection, and has become the standard protection system for series capacitor banks.

The capacitor bank is usually rated to withstand the line current for normal power flow conditions and power swing conditions. It is not economical to design the capacitors to withstand the currents and

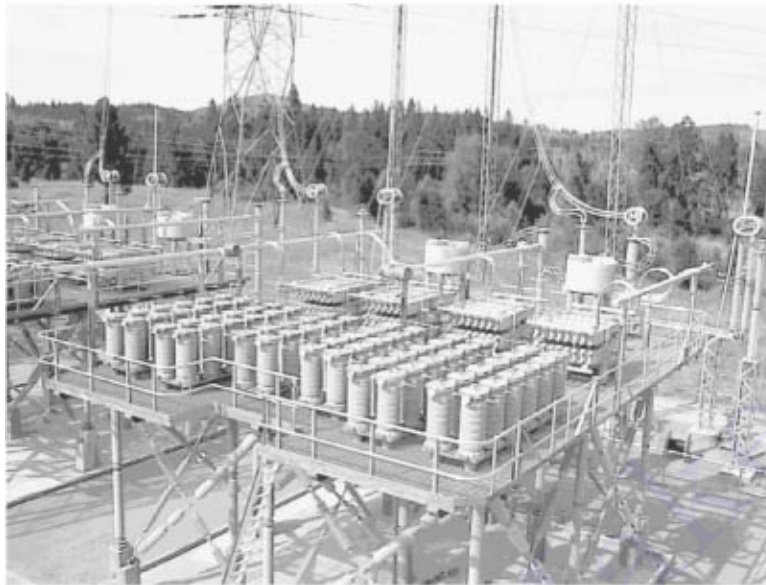


FIGURE 4.116 Aerial view of 500-kV series capacitor installation. (Photo courtesy of ABB.)

voltages associated with faults. Under these conditions capacitors are protected by a metal oxide varistor (MOV) bank. The MOV has a highly nonlinear resistive characteristic and conducts negligible current until the voltage across it reaches the protective level. For internal faults, which are defined as faults within the line section in which the series capacitor bank is located, fault currents can be very high. Under these conditions, both the capacitor bank and MOV will be bypassed by the “triggered spark gap.” The damping reactor (D) will limit the capacitor discharge current and damps the oscillations caused by spark gap operation or when the bypass breaker is closed. The amplitude, frequency of oscillation, and rate of damping of the capacitor discharge current will be determined by the circuit parameters, C (series capacitor), L (damping inductor), and resistance in the circuit, which in most cases is losses in the damping reactor.

A view of series capacitor bank installation is shown in [Fig. 4.116](#).

## Description of Main Components

### Capacitors

The capacitor bank for each phase consists of several capacitor units in series-parallel arrangement, to make up the required voltage, current, and Mvar rating of the bank. Each individual capacitor unit has one porcelain bushing. The other terminal is connected to the stainless steel casing. The capacitor unit usually has a built-in discharge resistor inside the case. Capacitors are usually all film design with insulating fluid that is non-PCB. Two types of fuses are used for individual capacitor units — internally fused or externally fused. Externally fused units are more commonly used in the U.S. Internally fused capacitors are prevalent in European installations.

### Metal Oxide Varistor (MOV)

A metal oxide varistor is built from zinc oxide disks in series and parallel arrangement to achieve the required protective level and energy requirement. One to four columns of zinc oxide disks are installed in each sealed porcelain container, similar to a high-voltage surge arrester. A typical MOV protection system contains several porcelain containers, all connected in parallel. The number of parallel zinc oxide disk columns required depends on the amount of energy to be discharged through the MOV during the worst-case design scenario. Typical MOV protection system specifications are as follows.

The MOV protection system for the series capacitor bank is usually rated to withstand energy discharged for all faults in the system external to the line section in which the series capacitor bank is located.

Faults include single-phase, phase-to-phase, and three-phase faults. The user should also specify the fault duration. Most of the faults in EHV systems will be cleared by the primary protection system in 3 to 4 cycles. Back-up fault clearing can be from 12 to 16 cycles duration. The user should specify whether the MOV should be designed to withstand energy for back-up fault clearing times. Sometimes it is specified that the MOV be rated for all faults with primary protection clearing time, but for only single-phase faults for back-up fault clearing time. Statistically, most of the faults are single-phase faults.

The energy discharged through the MOV is continuously monitored and if it exceeds the rated value, the MOV will be protected by the firing of a triggered air gap, which will bypass the MOV.

#### ***Triggered Air Gap***

The triggered air gap provides a fast means of bypassing the series capacitor bank and the MOV system when the trigger signal is issued under certain fault conditions (for example, internal faults) or when the energy discharged through the MOV exceeds the rated value. It typically consists of a gap assembly of two large electrodes with an air gap between them. Sometimes two or more air gaps in series can also be employed. The gap between the electrodes is set such that the gap assembly sparkover voltage without trigger signal will be substantially higher than the protective level of the MOV, even under the most unfavorable atmospheric conditions.

#### ***Damping Reactor***

A damping reactor is usually an air-core design with parameters of resistance and inductance to meet the design goal of achieving the specified amplitude, frequency, and rate of damping. The capacitor discharge current when bypassed by a triggered air gap or a bypass breaker will be damped oscillation with amplitude, rate of damping, and frequency determined by circuit parameters.

#### ***Bypass Breaker***

The bypass breaker is usually a standard line circuit breaker with a rated voltage based on voltage across the capacitor bank. In most of the installations, the bypass breaker is located separate from the capacitor bank platform and outside the safety fence. This makes maintenance easy. Both terminals of the breaker standing on insulator columns are insulated for the line voltage. It is usually a SF<sub>6</sub> puffer-type breaker, with controls at ground level.

#### ***Relay and Protection System***

The relay and protection system for the capacitor bank is located at ground level, in the station control room, with information from and to the platform transmitted via fiber-optic cables. The present practice involves all measured quantities on the platform being transmitted to ground level, with all signal processing done at ground level.

#### **Subsynchronous Resonance**

Series capacitors, when radially connected to the transmission lines from the generation near by, can create a subsynchronous resonance (SSR) condition in the system under some circumstances. SSR can cause damage to the generator shaft and insulation failure of the windings of the generator. This phenomenon is well-described in several textbooks, given in the reference list at the end of this section.

#### **Adjustable Series Compensation (ASC)**

The ability to vary the series compensation will give more control of power flow through the line, and can improve the dynamic stability limit of the power system. If the series capacitor bank is installed in steps, bypassing one or more steps with bypass breakers can change the amount of series compensation of the line. For example, as shown in Fig. 4.117, if the bank consists of 33% and 67% of the total compensation, four steps, 0%, 33%, 67%, and 100%, can be obtained by bypassing both banks, smaller bank (33%), larger bank (67%), and not bypassing both banks, respectively.

Varying the series compensation by switching with mechanical breakers is slow, which is acceptable for control of steady-state power flow. However, for improving the dynamic stability of the system, series compensation has to be varied quickly. This can be accomplished by thyristor controlled series compensation (TCSC).

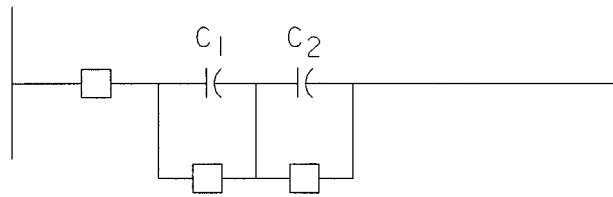


FIGURE 4.117 Breaker controlled variable series compensation.

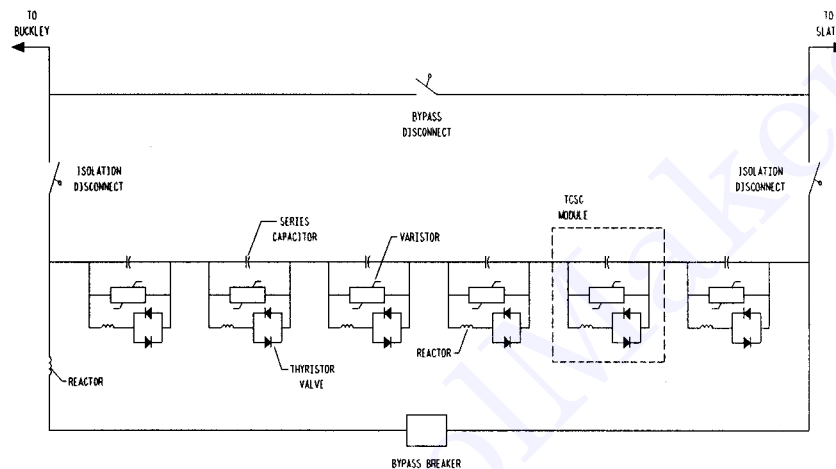


FIGURE 4.118 One-line diagram of TCSC installed at slatt substation.

### Thyristor Controlled Series Compensation (TCSC)

Thyristor controlled series compensation provides fast control and variation of the impedance of the series capacitor bank. To date (1999), three prototype installations, one each by ABB, Siemens, and the General Electric Company (GE), have been installed in the U.S. TCSC is part of the Flexible AC Transmission System (FACTS), which is an application of power electronics for control of the AC system to improve the power flow, operation, and control of the AC system. TCSC improves the system performance for subsynchronous resonance damping, power swing damping, transient stability, and power flow control.

The latest of the three prototype installations is the one at the Slatt 500-kV substation in the Slatt-Buckley 500-kV line near the Oregon-Washington border in the U.S. This is jointly funded by the Electric Power Research Institute (EPRI), the Bonneville Power Administration (BPA), and the General Electric Company (GE). A one-line diagram of the Slatt TCSC is shown in Fig. 4.118. The capacitor bank (8 ohms) is divided into six identical TCSC modules. Each module consists of a capacitor (1.33 ohms), back-to-back thyristor valves controlling power flow in both directions, a reactor (0.2 ohms), and a variator. The reactors in each module, in series with thyristor valves, limit the rate of change of current through the thyristors. The control of current flow through the reactor also varies the impedance of the combined capacitor-reactor combination, giving the variable impedance. When thyristor gating is blocked, complete line current flows through the capacitance only, and the impedance is 1.33 ohms capacitive (see Fig. 4.119a). When the thyristors are gated for full conduction (Fig. 119b), most of the line current flows through the reactor-thyristor branch (a small current flows through the capacitor) and the resulting impedance is 0.12 ohms inductive. If thyristors are gated for partial conduction only (Fig. 4.119c), circulating current will flow between capacitor and inductor, and the impedance can be varied from 1.33 ohms and 4.0 ohms, depending on the angle of conduction of the thyristor valves. The latter is called the vernier operating mode.

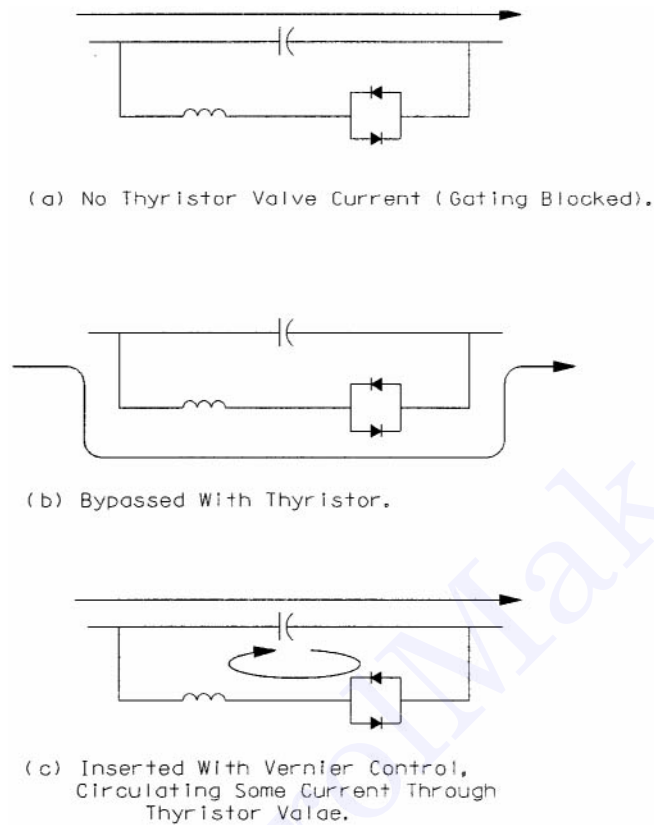


FIGURE 4.119 Current flow during various operating modes of TCSC.

The complete capacitor bank with all six modules can be bypassed by the bypass breaker. This bypass breaker is located outside the main capacitor bank platform, similar to the case for the conventional series capacitor bank. There is also a reactor connected in series with the bypass breaker to limit the magnitude of capacitor discharge current through the breaker. All reactors are of air-core dry-type design and rated for the full line current rating. Metal oxide varistors (MOV) connected in parallel with the capacitors in each module provide overvoltage protection. The MOV for a TCSC requires significantly less energy absorption capability than is the case for a conventional series capacitor of comparable size, because gating of thyristor valves provides quick protection for faulted conditions.

### STATic COMPensator (STATCOM)

STATCOM provides variable reactive power from lagging to leading, but with no inductors or capacitors for var generation. Reactive power generation is achieved by regulating the terminal voltage of the converter. The STATCOM consists of a voltage source inverter using gate turn-off thyristors (GTOs) which produces an alternating voltage source in phase with the transmission voltage, and is connected to the line through a series inductance which can be the transformer leakage inductance required to match the inverter voltage with line voltage. If the terminal voltage ( $V_t$ ) of the voltage source inverter is higher than the bus voltage, STATCOM generates leading reactive power. If  $V_t$  is lower than the bus voltage, STATCOM generates lagging reactive power. The performance is similar to the performance of a synchronous condenser (unloaded synchronous motor with varying excitation).

Reactive power generated or absorbed by STATCOM is not a function of the capacitor on the DC bus side of the inverter. The capacitor is rated to limit only the ripple current, and hence the harmonics in the output voltage.

The first demonstration STATCOM of  $\pm 100$  Mvar rating was installed at the Tennessee Valley Authority's Sullivan substation in 1994.

### Defining Terms

**Shunt capacitor bank:** A large number of capacitor units connected in series and parallel arrangement to make up the required voltage and current rating, and connected between the high-voltage line and ground, between line and neutral, or between line-to-line.

**Voltage flicker:** Commonly known as "flicker" and "lamp flicker," this is a rapid and frequent fluctuation of supply voltage that causes lamps to flicker. Lamp flicker can be annoying, and some loads are sensitive to these frequent voltage fluctuations.

**Subsynchronous resonance:** Per IEEE, subsynchronous resonance is an electric power system condition where the electric network exchanges energy with a turbine generator at one or more of the natural frequencies of the combined system below the synchronous frequency of the system.

### References

- Anderson, P.M., Agrawal, B.L., and Van Ness, J.E., *Subsynchronous Resonance in Power Systems*, IEEE Press, 1990.
- Anderson, P.M. and Farmer, R.G., *Series Compensation in Power Systems*, PBLSH! Inc. 1996.
- Gyugyi, L., Otto, R.A., and Putman, T.H., Principles and application of thyristor-controlled shunt compensators, *IEEE Trans. on Power Appar. and Syst.*, 97, 1935-1945, Sept/Oct 1978.
- Gyugyi, L. and Taylor, Jr., E.R., Characteristics of static thyristor-controlled shunt compensators for power transmission applications, *IEEE Trans. on Power Appar. and Syst.*, PAS-99, 1795-1804, 1980.
- Hammad, A.E., Analysis of power system stability enhancement by static VAR compensators, *IEEE Trans. on Power Syst.*, 1, 222-227, 1986.
- Miller, T.J.E., Ed., *Reactive Power Control in Electric Systems*, John Wiley & Sons, New York, 1982.
- Miske, Jr., S.A. et al., Recent Series Capacitor Applications in North America, Paper presented at *CEA Electricity '95 Vancouver Conference*, March 1995.
- Padiyar, K.R., *Analysis of Subsynchronous Resonance in Power Systems*, Kluwer Academic Publishers, 1999.
- Schauder, C. et al., Development of a  $\pm 100$  MVAR static condenser for voltage control of transmission systems, *IEEE Trans. on Power Delivery*, 10(3), 1486-1496, July 1995.